Tribology International 175 (2022) 107855

Contents lists available at ScienceDirect

Tribology International

journal homepage: www.elsevier.com/locate/triboint

Numerical modeling and design decisions for aerostatic bearings with relatively large nozzle sizes in Magic-Angle Spinning (MAS) systems

Rajdeep Deb [a,*], Andreas Hunkeler [a], Dirk Wilhelm [b], Patrick Jenny [c], Beat H. Meier [a]

[a] Laboratory of Physical Chemistry, ETH Zurich, Switzerland
[b] Institute of Applied Mathematics and Physics, ZHAW Winterthur, Switzerland
[c] Institute of Fluid Dynamics, ETH Zurich, Switzerland

ARTICLE INFO

Keywords:
Bearing number
Nozzle restriction parameter
Reynolds equation
Magic-angle spinning
Aerostatic bearing
Nozzle diameter

ABSTRACT

Numerical stability analysis for aerostatic bearings was performed to obtain optimized design parameters for small submillimeter to millimeter range diameter cylindrical rotors. Such rotors are used in nuclear magnetic resonance (NMR) application to rotate sample around an axis inclined by magic angle (54.74°) relative to the magnetic field direction at rotational frequencies of about 100 kHz (magic-angle spinning, MAS). The governing Reynolds equation for the fluid film between rotor and bearing was modified for small size aerostatic bearings with relatively large nozzle diameters. The modified Reynolds equation was solved using a finite-volume method to obtain pressure and film thickness around the rotor. This led to the solution of the maximum stable inertial force as a function of rotational frequency and design parameters. The comparison with aerostatic bearings with infinitesimal nozzle sizes was obtained for supported rotor weight and critical vibrational frequency of the rotor. The stable inertial force was found to correspond to a specific nozzle diameter and a specific rotor–bearing clearance. Numerical investigation also shows an enhancement of stable inertial force with decreasing nozzle number or increasing molecular mass of the impinging gas for a specific range of nozzle parameters. Experimental observations further confirmed the role of nozzle diameter, nozzle number and molecular weight of the gas in enhancing the rotor spinning frequency. Further, design decisions were made based on such analysis and were tested for varying rotor size and bearing properties. Using design optimization based on numerical simulation, the maximum frequency of rotation for a home-built 0.4 mm MAS rotor could be enhanced from 25 kHz up to 110 kHz, still below the extrapolation from large rotors.

1. Introduction

Solid-state NMR is an emerging analytical method for the characterization, at atomic resolution, of structure and dynamics of materials [1,2], and biomolecules [3,4]. To obtain highly resolved spectra, e.g. of proteins, the anisotropic spin interactions must be averaged out by mechanically rotating the sample around an axis inclined by an angle of 54.74°, which is termed as the magic-angle, with respect to the strong external magnetic field (10 T–28 T) applied in NMR experiments. In most high-resolution experiments, the rotation frequency in magic-angle spinning (MAS) [5] has to be at least comparable to the size of the anisotropic interactions to be averaged. In practice, MAS frequencies vary between 10 kHz and 160 kHz. Typically, e.g. for protein spectroscopy, the faster the spinning, the better the spectral resolution [6]. Spinning at 100 kHz and above have recently opened a whole new avenue of proton-detected solid-state NMR, in particular for biomolecules. [7,8]. Fast spinning was so far always achieved by reducing the rotor diameter [6]. A rotational frequency of 160 kHz was achieved with a rotor diameter of 0.5 mm [8]. As a next step it was attempted to use 0.4 mm rotor diameter. But this did not improve the frequency of rotation. Instead with initial bearing design, the rotor frequency could not be stabilized beyond 25 kHz. Therefore, the present study of the bearing design was initiated.

The sample to be investigated is contained in a cylindrical rotor sleeve with a diameter of 0.4 to 10 mm. Microturbines are used to drive the rotation of such MAS rotors [9]. Two bearings are used for MAS rotors as illustrated in Fig. 1. The position along the rotor axis is stabilized by an axial bearing (not shown). The bearing system provides support with minimum contact friction to the fast rotating MAS rotor and should have a minimal resisting torque. Such a bearing systems is a particular type of tribological application to support smooth running of devices, which have fast- and slow-moving parts. Such devices are characterized by additional unbalanced fluctuating forces, which can lead

* Corresponding author.
E-mail address: rajdeep.deb@phys.chem.ethz.ch (R. Deb).
URL: https://www.ssnmr.ethz.ch (R. Deb).

https://doi.org/10.1016/j.triboint.2022.107855
Received 23 April 2022; Received in revised form 22 July 2022; Accepted 4 August 2022
Available online 13 August 2022

List of Abbreviations

A_n	Bearing nozzle area, $A_n = \left(\frac{\pi d_n^2}{4}\right)$
$\bar{A}_n$	Dimensionless bearing nozzle area, $\bar{A}_n = \frac{A_n}{LR_b}$
B_{ij}, $\bar{B}_{ij}$	Bearing damping, $\bar{B}_{ij} = (c\omega_r B_{ij})/(2P_a LR_b)$
C_b	Bearing center position
C_d	Nozzle discharge coefficient
C_j	Rotor center position
c	Clearance between rotor and bearing
c_β	Exponential growth rate of displacement amplitude
D_r	Rotor diameter
d_n	Nozzle diameter
$\mathrm{d}V$	Differential area, $\mathrm{d}V = \mathrm{d}\theta\mathrm{d}\bar{z}$
e, ε	Eccentricity, $\varepsilon = e/c$
e_0, ε_0	Equilibrium eccentricity, $\varepsilon_0 = e_0/c$
F_i, $\bar{F}_i$	Force along ith direction, $\bar{F}_i = F_i/(2P_a LR_b)$
g	Acceleration due to gravity
$h, \bar{h}$	Film thickness, $\bar{h} = h/c$
$h_0, \bar{h}_0$	Equilibrium Film thickness, $\bar{h}_0 = h_0/c$
$\hat{j}$	Imaginary root of unity
m_r	Rotor mass
K_{ij}, $\bar{K}_{ij}$	Bearing stiffness, $\bar{K}_{ij} = (cK_{ij})/(2P_a LR_b)$
L	Bearing length
L_j	Rotor length
$\dot{m}$	Nozzle mass flow rate
$\bar{M}$	Dimensionless inertial force $\bar{M} = \left(\frac{0.5m_r\omega_r^2 c}{2P_a LR_b}\right)$
$\dot{m}_{nd}$	Non-dimensional mass flow rate through nozzle
N_r	Number of nozzles in bearing
P_a	Ambient pressure
p_s, $\bar{P}_s$	Nozzle pressure, $\bar{P}_s = p_s/P_a$
p, $\bar{P}$	Fluid pressure, $\bar{P} = p/P_a$
$\bar{P}_\varepsilon$, $\bar{P}_\phi$	Dynamic pressure perturbation due to small change in ε and ϕ
Q_r	Source term due to nozzle mass flow in non-dimensionalized Reynolds equation
R_b	Bearing radius
R_j	Rotor radius
R^0	Universal gas constant per unit mass
T^0	Nozzle gas temperature
U_0	Relative speed between bearing and rotor wall
S^{nozzle}	Source term due to each nozzle mass flow in Reynolds equation
W, $\bar{W}$	Rotor load, $\bar{W} = W/(2P_a LR_b)$
$\bar{W}_r$	Dimensionless rotor weight stabilized by each bearing, $\bar{W}_r = \left(\frac{0.5m_r g\sin\theta_{mas}}{2P_a LR_b}\right)$
x, $\bar{x}$	Space coordinate along direction perpendicular to rotor axis and weight axis, $\bar{x} = x/L$
y, $\bar{y}$	Space coordinate along weight axis, $\bar{y} = y/L$
z, $\bar{z}$	Space coordinate along the rotor shaft, $\bar{z} = z/L$
$\bar{X}$, $\bar{Y}$	The amplitude of vibration along $\bar{x}, \bar{y}$ direction respectively for rotor center
μ	Dynamic viscosity
ω_r	Rotation frequency of the rotor
Λ	Bearing number $\Lambda = \left(\frac{6\mu\omega_r R_b^2}{P_a c^2}\right)$
Λ_{max}	Maximum experimentally obtained Bearing number
Λ_{sim}	Bearing number used in numerical simulation
λ	Aspect ratio, $\lambda = L/2R_b$
∇	Gradient operator, $\nabla = \left[\frac{\partial}{\partial\theta} \quad \frac{\partial}{\partial\bar{z}}\right]^T$
ϕ	Attitude angle
ϕ_0	Equilibrium Attitude angle
ρ	Gas density
$\theta, \bar{\theta}$	Angular coordinate along the bearing perimeter with respect to the weight axis, $\bar{\theta} = (\theta - \phi_0)$
θ_n	Angular position of the nozzle
κ	Specific heat ratio for nozzle inlet gas
θ_{MAS}	Angle for magic-angle spinning, $\theta_{MAS} = 54.74°$
Ω	Whirl rotation frequency
γ	Whirl ratio, $\gamma = \Omega/\omega_r$
γ_c	Critical whirl ratio
τ	Dimensionless time, $\tau = \Omega t$
ε_p	Small perturbation magnitude of eccentricity ratio
ϕ_p	Small perturbation magnitude of attitude angle
$\triangle\theta$	Grid size along θ direction
$\triangle\bar{z}$	Grid size along $\bar{z}$ direction

to vibrations of the rotor. Bearing systems minimize such vibrations by providing stiffness and damping to the rotor motion. Friction control, vibration control and load support are therefore essential requirements for bearing devices. Different types of bearings such as magnetic bearings and lubrication bearings are used in different machines [10]. The use of magnetic bearings in MAS systems is prohibited due to the presence of a strong external magnetic field. Further, the presence of magnetic parts can distort the homogeneous magnetic field which is a prerequisite for the NMR experiment. Therefore, lubrication bearings are used in MAS devices. Traditional lubrication materials such as oil cannot be used in MAS devices due to interference with the NMR experiments. Therefore, air or inert gases such as Nitrogen or Helium are used as lubrication fluid. Rotating devices create non-symmetrical pressure distributions in the surrounding fluid, which provide restoring forces against device vibrations. Such self-compliant bearings are called aerodynamic bearings. However, for high rotation frequency, aerodynamic bearings are not adequate to stabilize rotor vibrations and high-pressure gas feeds are needed to stabilize the rotor and to provide enough load support. Bearings with such thrust feeds of air or other gases are described as aerostatic bearings or thrust bearings [11,12]. The critical design parameters of aerostatic bearings are bearing length (L), gap between rotor and bearing (described as clearance (c)), the orifice hole diameter (d_n) and the number of orifice holes (N_r). In the rest of the paper, the term nozzle is used to represent orifice holes. Further, the bearing radius (R_b) also plays an important role in bearing design. The weight of the rotating device leads to a shift in the rotor center location relative to the bearing center as portrayed in Fig. 2. The magnitude of this displacement is denoted as eccentricity (e). The symmetrical pressure distribution around the rotor is disturbed by this rotor displacement, which results in a net force balancing the rotor weight or any other external force, such that the rotor floats within the bearing.

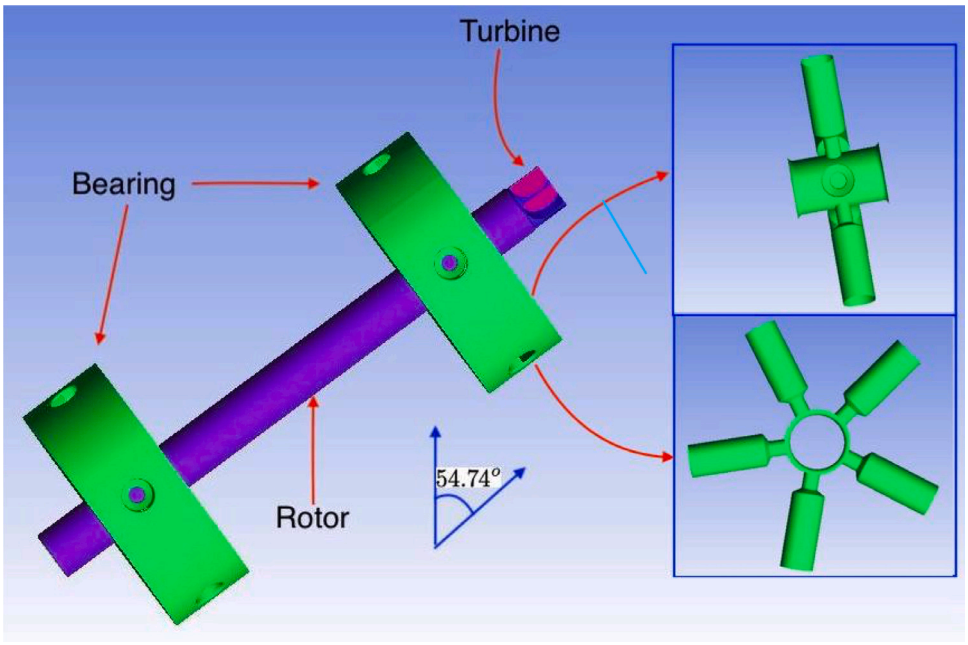

Fig. 1. The configuration of MAS rotor and bearing system.

Computational fluid dynamics (CFD) analyses of MAS turbines are reported in [9,13–15]. The CFD simulation in [9] shows that the main stability criteria for MAS turbines are rotor speed and turbine stability; and not the turbine performance efficiency. The corresponding stability of the rotor is dependent on the applied bearing system. This therefore requires a closer look into the stability analysis of aerostatic bearings. Rotor sizes of few millimeters or even less than a millimeter are common in MAS applications. Design principles for NMR rotors to achieve maximum frequency of rotation are discussed by Doty et al. [16]. In this paper, the optimal bearing design principles are obtained based on the asymmetric load distribution at rotation frequencies around $3-6$ kHz. Such theoretical analyses are based on large diameter rotor size and cannot be scaled down to smaller rotors due to limitations of manufacturing and stability issues. However, for fast MAS rotation, the rotor diameter and therefore bearing radius are reduced to submillimeter range [17]. Due to design limitations, the ratio of nozzle diameter to bearing radius (d_n/R_b) is relatively large for aerostatic bearing used for MAS compared to ones used for large rotors. The usual Reynolds equation solved for bearing studies assumes an infinitesimal nozzle diameter $(d_n/R_b \ll 1)$ [18]. In this paper, this assumption is relaxed by allowing for finite nozzle diameters, which results in a modified Reynolds equation. Further, for the numerical calculations the grid around the nozzles is resolved. In Appendix A, the modified Reynolds equation is derived for large nozzle size. The modified Reynolds equation is solved using a finite-volume method to obtain static equilibrium and dynamic inertial force for the rotor–bearing system.

The static equilibrium of the bearing–rotor system is characterized by initial eccentricity (e_0) and attitude angle (ϕ_0) as depicted in the Fig. 2(*a*). The attitude angle is defined as the angular position of rotor center relative to the axis passing through bearing center along the direction of the gravitational force of the rotor. The static equilibrium characteristics are governed by the pressure distribution of fluid around the rotor and the gravitational force. The torque required to balance the resistance torque from the bearing is usually provided by high-pressure fluid feed to turbine blades attached to the rotor [13]. In order to stabilize the device along the direction of the rotation axis, a thrust bearing is applied in the back end of the rotor with nozzle feed along the axis of rotation. The high-pressure gas feed on the turbine blades also provides additional fluctuating forces perpendicular to the axis of rotation. These forces disturb the static equilibrium position of the rotor inside the bearing system. Therefore, movement occurs for the rotor in the plane perpendicular to the axis of rotation. The pressure perturbations, in the fluid filled gap surrounding the rotor provides the resistance to such movement of the rotor. This resistance can be modeled as stiffness and damping provided by the fluid film surrounding the rotor as illustrated in Fig. 2(*b*). The limited damping is one of the reasons for enhanced instability of aerostatic or aerodynamic bearings [19,20]. Two types of instability are observed in bearing system. These are respectively pneumatic hammer instability and whirl instability. Pneumatic hammer is caused mainly due to externally applied force resonance with stiffness provided by fluid film. The whirl instability, which is usually of the order of half the value of rotation speed, is governed mainly by a limited damping effect. Further details of different form of instability developed in such bearing system are described in details in [19]. The variation of resistance force due to fluid film with the displacement of rotor center provides the stiffness and damping calculation. This resistance force is therefore estimated to describe the main source of such instabilities and vibrations [12,21]. The numerical estimation of this resistance force as a function of design parameters provides the controlling features for the dynamics of vibrations [12,22]. Nozzle geometry and clearance value of the rotor–bearing system can be optimized to minimize rotor vibrations. The analysis of these properties for critical vibration frequencies is therefore important to design a bearing for a specific rotor size and rotor speed. For an infinitesimally small nozzle size relative to the bearing size, the numerical analysis of the static equilibrium and dynamic properties of the bearing are reported in various publications, e.g. in [22–33]. These analyses are useful for relatively large turbine or rotor diameter (>10 mm). To construct MAS rotors, in particular for proton-detection experiments in proteins, rotation at about ($\sim$100 kHz) or higher is desirable. This is only possible with rotors of a diameter below 1 mm. In this paper, the influence of design parameters in stability characteristics of bearing used in such MAS rotors is systematically analyzed. The analysis suggests suitable design properties for the bearing to maximize the stabilizing inertial force. The dependence predicted is compared to the behavior of a test system realized for a rotation frequency of 110 kHz.

Section 2 describes the governing equations for static and dynamic studies of bearing–rotor systems. Section 3 describes the linear stability analysis of the governing Reynolds equations, which leads to

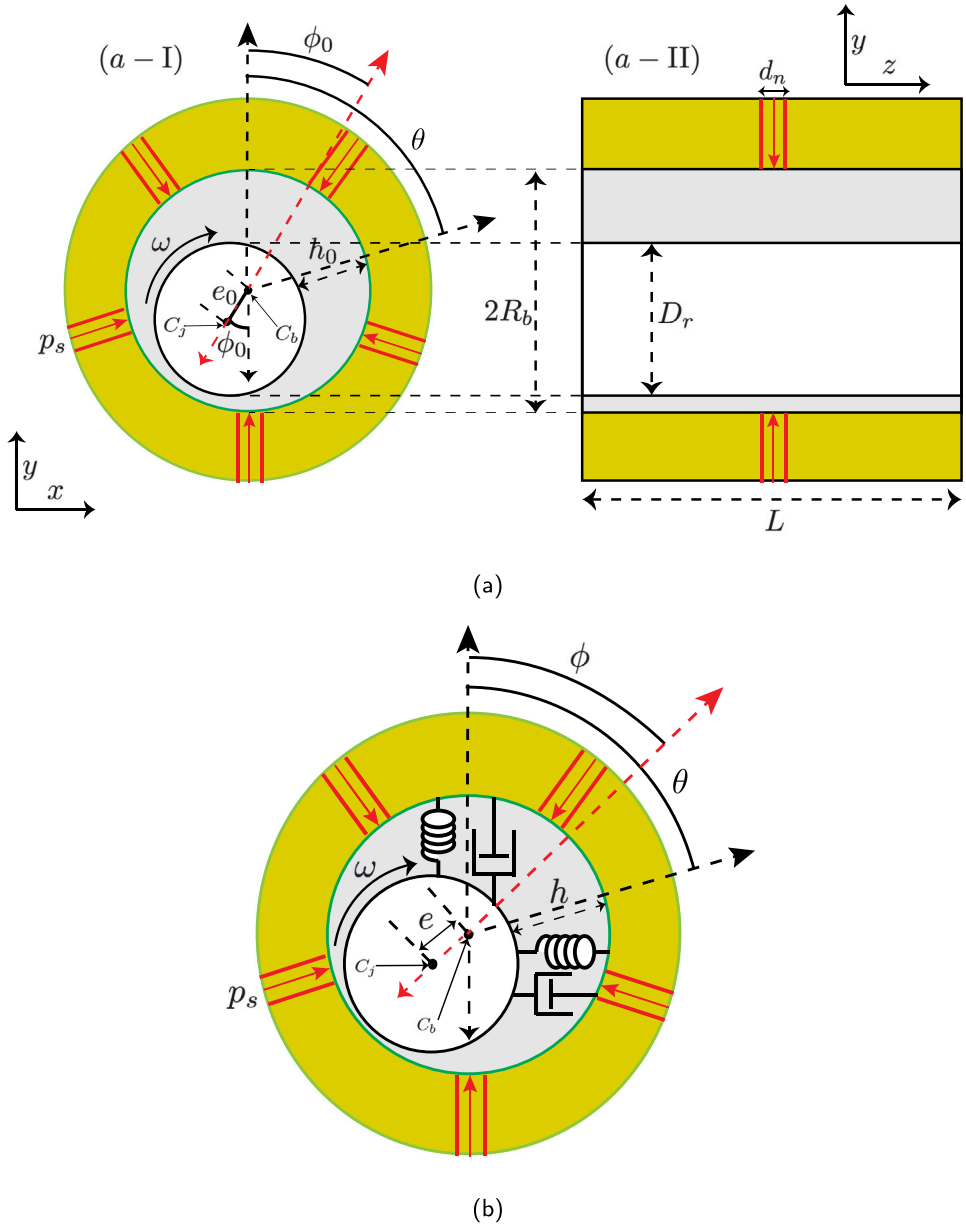

Fig. 2. Simple geometric representation of the aerostatic bearing. Part (*a*) depicts the static equilibrium configuration of the rotor–bearing system. The inner circle in the top left and bottom figure (*b*) represent the rotor with a diameter of D_r. The shaded gray region in all three figures represents the fluid film. The green region represents the bearing with a radius of R_b. The red channels represent bearing nozzles with a diameter of d_n. The top left and right figure represents the front and side view of the rotor–bearing system. The bottom figure (*b*) represents the perturbed configuration of the rotor–bearing system with imaginary stiffness and damping provided by the fluid film. (For interpretation of the references to color in this figure legend, the reader is referred to the web version of this article.)

the estimation of stiffness and damping calculations for the bearing. Section 4 describes the numerical finite-volume method applied to resolve the Reynolds equation. Section 5 describes the results of static load calculations and stability analysis results to obtain the critical frequency, stiffness and damping parameters. Section 5.4 describes the experimental results with different bearing designs. Finally, in Section 6 conclusions are drawn for the design of aerostatic bearings with small rotors and fast rotation. The design principles discussed in [16] concentrate on large rotors. There the speed limitations based on maximum turbine power generation are analyzed. Here, it is shown that for small rotors with high-speed motion the speed is also severely limited by the bearing design. There exists a range of maximum rotational frequencies, which is driven by bearing stabilizing properties.

2. Governing equations

Fig. 2(*a*) depicts the rotor–bearing system with initial static equilibrium configuration (e_0, ϕ_0). The top view of the rotor–bearing system looking along the bearing axis is sketched on the left. The right part of Fig. 2(*a*) depicts the side view of the rotor–bearing system. The variables R_b, D_r, L and d_n denote the bearing radius, rotor diameter, bearing length and bearing nozzle diameter respectively. The variables C_j and C_b represents the rotor and bearing centers and e_0 is the equilibrium eccentricity of the rotor–bearing configuration, which represents the displacement of the rotor center from bearing center. Fig. 2(*b*) depicts the imaginary spring and damper system corresponding to the fluid film. The eccentricity ratio ε is defined as the ratio of eccentricity e to clearance $c = \left(R_b - \frac{D_r}{2}\right)$. The term ε_0 defines the initial static equilibrium eccentricity ratio. Given the angular position θ, as represented

in Fig. 2(*a*), the fluid film thickness and the dimensionless film thickness are given as

$$h_0 = c + e_0 \cos(\theta - \phi_0) \tag{1}$$

$$\text{and } \bar{h}_0 = \left(h_0/c\right) = 1 + \varepsilon_0 \cos(\theta - \phi_0) \tag{2}$$

respectively. This asymmetrical film thickness along the angular coordinate θ leads to the asymmetrical pressure distribution, which provides the hydrodynamic force balance perpendicular to the bearing axis. This term is denoted as rotor load. The nozzle entries illustrated by red channels in Fig. 2 further provide high-pressure fluid flow to stabilize the rotor load. The stiffness and damping matrices K_{ij} and B_{ij} are defined as

$$K_{ij} = -\frac{\partial F_j}{\partial r_i} \tag{3}$$

$$\text{and } B_{ij} = -\frac{\partial F_j}{\partial \dot{r}_i}, \tag{4}$$

where F_i defines the applied force along the ith coordinate direction on the rotor due to pressure distribution around the rotor, and terms r_j and $\dot{r}_j$ define the position and velocity of the rotor center respectively along the jth direction with $i, j \in \{1, 2, 3\}$.

The rotor rotates with an angular frequency of ω_r. Following are a few important numbers, which govern the rotor–bearing system's static and dynamic equilibrium:

$$\text{Bearing number, } \Lambda = \frac{6\mu\omega_r R_b^2}{P_a c^2} \tag{5}$$

$$\text{Dimensionless inertial force, } \bar{M} = \frac{0.5 m_r \omega_r^2 c}{2 P_a L R_b} \tag{6}$$

$$\text{Aspect ratio, } \lambda = \frac{L}{2R_b} \tag{7}$$

$$\text{Whirl ratio, } \gamma = \frac{\Omega}{\omega_r} \tag{8}$$

The terms m_r, μ and P_a denote the rotor mass, fluid film viscosity and the ambient pressure at the bearing exit. The term Ω represents frequency of externally imposed vibration. The term Λ is denoted as bearing number and represents the dimensionless relative wall speed of the rotor–bearing system, where rotor wall speed $(\omega_r R_b)$ is scaled with a reference speed of $\left(P_a c^2/6\mu R_b\right)$. Therefore, the bearing number also defines the non-dimensional operating point for rotor speed independent of the rotor geometry. The term $\bar{M}$ is the inertial force and plays a critical role in stability analysis of the system. The term λ defines the geometrical aspect ratio of the bearing.

2.1. Nozzle size adjustment in Reynolds equation

In cylindrical coordinates, the Reynolds equation for the fluid film between rotor and bearing with infinitesimally small nozzles $(d_n/R_b \ll 1)$ is given as

$$\frac{1}{R_b^2}\frac{\partial}{\partial\theta}\left(\frac{\rho h^3}{12\mu}\frac{\partial p}{\partial\theta}\right) + \frac{\partial}{\partial z}\left(\frac{\rho h^3}{12\mu}\frac{\partial p}{\partial z}\right) = \frac{1}{2}\frac{\partial\left(\rho h U_0\right)}{R_b \partial\theta} + \frac{\partial(\rho h)}{\partial t} - S^{nozzle}, \tag{9}$$

where the terms ρ, p and h respectively denote fluid density, fluid pressure and gap size between rotor and bearing. The terms U_0 and S^{nozzle} respectively denote the relative speed between bearing and rotor wall and the source term in the Reynolds equation due to the nozzles. The terms θ and z denote angular and axial coordinates of the rotor surface. With the approximation of infinitesimal nozzles, the source term S^{nozzle} is replaced by singularities $\sum_{k=1}^{N_r} \delta(\mathbf{x} - \mathbf{x}_{n_k})\dot{m}_{nk}$ with $\dot{m}_{nk}$ representing mass flow through the kth nozzle located at position $\mathbf{x}_{n_k}$. Therefore, integrating the term S^{nozzle} over a small area A such that $A_n \in A$, where A_n represents the area of the nozzle located at the position $\mathbf{x}_{n_k}$, leads to

$$\int_A S^{nozzle} \mathrm{d}A = \dot{m}_{nk}. \tag{10}$$

For simplicity of the notation and calculations, in the rest of the paper the subscript nk is removed for the term mass flow rate through the nozzle i.e. $\dot{m}_{nk} = \dot{m}$. The nozzle mass flow model obtained from [34] is given as

$$\dot{m} = \frac{C_d A_n p_s \delta}{\sqrt{R^0 T^0}}, \tag{11}$$

where $A_n = \left(\pi d_n^2/4\right)$ for a circular nozzle with nozzle diameter d_n. The terms C_d, R^0 and T^0 in Eq. (10) are nozzle flow coefficient, universal gas constant per unit mass and temperature of the inlet gas respectively. The term δ in Eq. (11), as defined in [24,34], is given as

$$\delta = \begin{cases} \sqrt{\frac{2\kappa}{(\kappa-1)}\left[\left(\frac{p_r}{p_s}\right)^{2/\kappa} - \left(\frac{p_r}{p_s}\right)^{(\kappa+1)/\kappa}\right]} & \text{for subsonic conditions and} \\ \sqrt{\kappa\left(\frac{2}{\kappa+1}\right)^{\frac{(\kappa+1)}{(\kappa-1)}}} & \text{for supersonic conditions.} \end{cases} \tag{12}$$

The term κ in Eq. (12) is the ratio of constant pressure specific heat capacity to constant volume specific heat capacity for the inlet gas. The terms p_r and p_s respectively represent the local fluid pressure at the nozzle location and nozzle inlet pressure. Using the characteristic scales L, c, P_a and $1/\Omega$ for non-dimensionalization of z, h, p and t, the dimensionless Reynolds equation for infinitesimal nozzles yields

$$\frac{\partial}{\partial\theta}\left[\bar{h}^3\frac{\partial\bar{P}^2}{\partial\theta}\right] + \frac{1}{4\lambda^2}\frac{\partial}{\partial\bar{z}}\left[\bar{h}^3\frac{\partial\bar{P}^2}{\partial\bar{z}}\right] = 2\Lambda\frac{\partial}{\partial\theta}\left(\bar{P}\bar{h}\right) + 4\gamma\Lambda\frac{\partial}{\partial\tau}\left(\bar{P}\bar{h}\right) - \frac{1}{8\lambda}\bar{Q}_r \tag{13}$$

where $\bar{z} = z/L$, $\bar{h} = h/c$, $\bar{P} = p/P_a$ and $\tau = \Omega t$. The dimensionless source term $\bar{Q}_r$ due to nozzle mass flow is such that

$$\int_{\bar{A}} \bar{Q}_r \mathrm{d}\theta \mathrm{d}\bar{z} = \Gamma_0 \bar{P}_s \delta \tag{14}$$

$$\text{where } \Gamma_0 = \frac{24\mu\pi d_n^2 C_d \sqrt{R^0 T^0}}{P_a c^3}. \tag{15}$$

The term $\bar{A}$ represents an area covering an infinitesimal nozzle scaled by $\left(R_b L\right)$. The terms $\mathrm{d}\theta$ and $\mathrm{d}\bar{z}$ represent the differential coordinates in θ and $\bar{z}$ direction. Typically a nozzle diameter size of $0.1 - 0.2$ mm is used for a bearing size of $5 - 10$ mm diameter $(d_n/R_b = 0.02)$ and a similar order for the bearing length [16]. For such scenarios the nozzle entry size can be assumed to be infinitesimal compared to the bearing domain size. However, in high-speed MAS systems, the nozzle diameter is of the order of bearing size $(d_n/R_b \approx 0.33)$. Therefore, the Reynolds equation has to be modified to include the effect of finite sized nozzle diameter in the source term. The systematic derivation of the Reynolds equation from continuity and Poiseuille equations is presented in the appendix (*A*). The nozzle source term for finite sized nozzles is modeled as

$$S^{nozzle} = \frac{\mathrm{d}\dot{m}}{\mathrm{d}A_n}, \tag{16}$$

where A_n represents the nozzle area. Using relation (11) and (16) in Eq. (9), the governing dimensionless Reynolds equation for relatively large nozzle size is given as

$$\frac{\partial}{\partial\theta}\left[\bar{h}^3\frac{\partial\bar{P}^2}{\partial\theta}\right] + \frac{1}{4\lambda^2}\frac{\partial}{\partial\bar{z}}\left[\bar{h}^3\frac{\partial\bar{P}^2}{\partial\bar{z}}\right] = 2\Lambda\frac{\partial}{\partial\theta}\left(\bar{P}\bar{h}\right) + 4\gamma\Lambda\frac{\partial}{\partial\tau}\left(\bar{P}\bar{h}\right) - \left(\frac{R_b^2}{\pi d_n^2}\right)\bar{Q}_r^{finite} \tag{17}$$

$$\text{where } \bar{Q}_r^{finite} = \Gamma_0 \bar{P}_s \delta \tag{18}$$

The detailed derivation of dimensionless Reynolds equation for finite sized nozzles is presented in appendix (*A*). In the rest of the paper, the infinitesimal nozzle term is used for $(d_n/R_b) \to 0$ and the large nozzle term is used for finite values of (d_n/R_b). The term Γ_0 is called nozzle restriction number. This non-dimensional term assembles all the contributions from nozzle, bearing geometry and the gas property in the source term (due to mass flow through nozzle) of dimensionless Reynold's equation.

3. Linear stability analysis of the bearing

In the following it is considered a linear stability analysis with two degrees of freedom, because of the long rotor length compared to the clearance (c) [27,35]. A perturbation about an equilibrium position (ε_0, ϕ_0) is obtained as whirl rotation with a frequency of Ω and a whirl ratio of $\gamma = (\Omega/\omega_r)$. The corresponding film thickness and fluid film pressure are given as

$$\bar{h} = \bar{h}_0 + \varepsilon_p \exp(\hat{j}\tau)\cos\bar{\theta} + \varepsilon_0\phi_p \exp(\hat{j}\tau)\sin\bar{\theta} \tag{19}$$

$$\text{and } \bar{P} = \bar{P}_0 + \varepsilon_p \exp(\hat{j}\tau)\bar{P}_\varepsilon + \varepsilon_0\phi_p \exp(\hat{j}\tau)\bar{P}_\phi, \tag{20}$$

where $\bar{\theta} = (\theta - \phi_0)$. The terms $\bar{P}_\varepsilon$ and $\bar{P}_\phi$ represent the dynamic pressure-perturbation components and $\hat{j}$ denotes the root of minus unity i.e. $\hat{j}^2 = -1$. The terms ε_p and ϕ_p define the magnitude of the perturbation function around the equilibrium position (ε_0, ϕ_0). Inserting the solutions (19) and (20) into the Reynolds Eqs. (13) and (17), the governing equations for perturbation pressure are obtained as in [35]. In this paper, a systematic derivation of the perturbation equation is given in appendix *B*. The perturbed pressure Eq. (20) can be reformulated as

$$\bar{P} = \bar{P}_0 + \boldsymbol{\varepsilon_p} Re[\bar{P}_\varepsilon] + \dot{\boldsymbol{\varepsilon}}_{\boldsymbol{p}} Im[\bar{P}_\varepsilon] + \varepsilon_0\boldsymbol{\phi_p} Re[\bar{P}_\phi] + \varepsilon_0\dot{\boldsymbol{\phi}}_{\boldsymbol{p}} Im[\bar{P}_\phi], \tag{21}$$

where

$$\boldsymbol{\varepsilon_p} = \varepsilon_p \exp(\hat{j}\tau),\ \dot{\boldsymbol{\varepsilon}}_{\boldsymbol{p}} = \frac{\partial \boldsymbol{\varepsilon_p}}{\partial\tau} = \hat{j}\varepsilon_p \exp(\hat{j}\tau) \tag{22}$$

$$\text{and } \boldsymbol{\phi_p} = \phi_p \exp(\hat{j}\tau) \text{ and } \dot{\boldsymbol{\phi}}_{\boldsymbol{p}} = \frac{\partial \boldsymbol{\phi_p}}{\partial\tau} = \hat{j}\phi_p \exp(\hat{j}\tau). \tag{23}$$

The terms $Re[\bar{P}_\varepsilon]$, $Re[\bar{P}_\phi]$, $Im[\bar{P}_\varepsilon]$ and $Im[\bar{P}_\phi]$ represent the real and imaginary parts of the perturbation pressure components $\bar{P}_\varepsilon$ and $\bar{P}_\phi$. Solutions for dynamic-pressure perturbation components lead to the estimation of dimensionless stiffness and damping provided by the aerostatic bearing as follows:

$$\begin{bmatrix} \bar{K}_{\varepsilon\varepsilon} & \bar{K}_{\phi\varepsilon} \\ \bar{K}_{\varepsilon\phi} & \bar{K}_{\phi\phi} \end{bmatrix} = -Re\left[\frac{1}{2}\int_0^1\int_0^{2\pi} \begin{bmatrix} \cos\bar{\theta} & \cos\bar{\theta} \\ \sin\bar{\theta} & \sin\bar{\theta} \end{bmatrix} \begin{bmatrix} \bar{P}_\varepsilon & 0 \\ 0 & \bar{P}_\phi \end{bmatrix} \mathrm{d}\bar{\theta}\mathrm{d}\bar{z}\right], \tag{24}$$

$$\begin{bmatrix} \bar{B}_{\varepsilon\varepsilon} & \bar{B}_{\phi\varepsilon} \\ \bar{B}_{\varepsilon\phi} & \bar{B}_{\phi\phi} \end{bmatrix} = -Im\left[\frac{1}{2}\int_0^1\int_0^{2\pi} \begin{bmatrix} \cos\bar{\theta} & \cos\bar{\theta} \\ \sin\bar{\theta} & \sin\bar{\theta} \end{bmatrix} \begin{bmatrix} \bar{P}_\varepsilon & 0 \\ 0 & \bar{P}_\phi \end{bmatrix} \mathrm{d}\bar{\theta}\mathrm{d}\bar{z}\right]. \tag{25}$$

The terms $Re[]$ and $Im[]$ in Eqs. (24) and (25) represent the operators to obtain the real and imaginary parts of a complex number. The reference parameters used for non-dimensionalization of stiffness and damping are $(2P_aLR_b/c)$ and $\left(2P_aLR_b/(c\omega_r)\right)$, respectively. Using coordinate transformation from (ε, ϕ) to fixed axes ($\bar{x}$, $\bar{y}$), stiffness and damping along fixed coordinates ($\bar{x}$, $\bar{y}$) are given as

$$\begin{bmatrix} \bar{K}_{yy} & \bar{K}_{xy} \\ \bar{K}_{yx} & \bar{K}_{xx} \end{bmatrix} = \begin{bmatrix} \cos\phi_0 & -\sin\phi_0 \\ \sin\phi_0 & \cos\phi_0 \end{bmatrix} \begin{bmatrix} \bar{K}_{\varepsilon\varepsilon} & \bar{K}_{\phi\varepsilon} \\ \bar{K}_{\varepsilon\phi} & \bar{K}_{\phi\phi} \end{bmatrix} \begin{bmatrix} \cos\phi_0 & \sin\phi_0 \\ -\sin\phi_0 & \cos\phi_0 \end{bmatrix} \tag{26}$$

and

$$\begin{bmatrix} \bar{B}_{yy} & \bar{B}_{xy} \\ \bar{B}_{yx} & \bar{B}_{xx} \end{bmatrix} = \begin{bmatrix} \cos\phi_0 & -\sin\phi_0 \\ \sin\phi_0 & \cos\phi_0 \end{bmatrix} \begin{bmatrix} \bar{B}_{\varepsilon\varepsilon} & \bar{B}_{\phi\varepsilon} \\ \bar{B}_{\varepsilon\phi} & \bar{B}_{\phi\phi} \end{bmatrix} \begin{bmatrix} \cos\phi_0 & \sin\phi_0 \\ -\sin\phi_0 & \cos\phi_0 \end{bmatrix}. \tag{27}$$

For the rotor center, the governing equations of motion with two bearings are given as

$$m_r\frac{\mathrm{d}^2x}{\mathrm{d}t^2} + 2B_{xx}\frac{\mathrm{d}x}{\mathrm{d}t} + 2B_{yx}\frac{\mathrm{d}x}{\mathrm{d}t} + 2K_{xx}x + 2K_{yx}y = 0 \tag{28}$$

$$\text{and } m_r\frac{\mathrm{d}^2y}{\mathrm{d}t^2} + 2B_{xy}\frac{\mathrm{d}y}{\mathrm{d}t} + 2B_{yy}\frac{\mathrm{d}y}{\mathrm{d}t} + 2K_{xy}x + 2K_{yy}y = 0. \tag{29}$$

Using non-dimensionalization of space, time and force variables using characteristic parameters c, $(1/\Omega)$ and $(2P_aLR_b)$, the Eqs. (28) and (29) become

$$\begin{bmatrix} \bar{M}\gamma^2 & 0 \\ 0 & \bar{M}\gamma^2 \end{bmatrix} \begin{bmatrix} \ddot{\bar{x}} \\ \ddot{\bar{y}} \end{bmatrix} + \begin{bmatrix} \bar{B}_{xx}\gamma & \bar{B}_{yx}\gamma \\ \bar{B}_{xy}\gamma & \bar{B}_{yy}\gamma \end{bmatrix} \begin{bmatrix} \dot{\bar{x}} \\ \dot{\bar{y}} \end{bmatrix} + \begin{bmatrix} \bar{K}_{xx} & \bar{K}_{yx} \\ \bar{K}_{xy} & \bar{K}_{yy} \end{bmatrix} \begin{bmatrix} \bar{x} \\ \bar{y} \end{bmatrix} = 0, \tag{30}$$

where $\bar{x} = x/c$, $\dot{\bar{x}} = \frac{\mathrm{d}\bar{x}}{\mathrm{d}\tau}$ and $\ddot{\bar{x}} = \frac{\mathrm{d}^2\bar{x}}{\mathrm{d}\tau^2}$. Assuming a perturbation function for each component of the fluctuation with a whirl frequency Ω, the perturbation functions are given as

$$\bar{x} = \bar{X}\exp(s\tau) \tag{31}$$

$$\text{and } \bar{y} = \bar{Y}\exp(s\tau), \tag{32}$$

where $s = \left((c_\beta/\Omega) \pm \hat{j}\right)$. The terms $\bar{X}$ and $\bar{Y}$ represent the initial amplitudes of the fluctuating dimensionless rotor center components $\bar{x}$ and $\bar{y}$, respectively. The term c_β represents the exponential growth rate of the displacement amplitude. Setting the solutions (31) and (32) into Eq. (30), the relation

$$\begin{bmatrix} \left(\bar{M}\gamma^2s^2 + \bar{B}_{xx}\gamma s + \bar{K}_{xx}\right) & \left(\bar{B}_{yx}\gamma s + \bar{K}_{yx}\right) \\ \left(\bar{B}_{xy}\gamma s + \bar{K}_{xy}\right) & \left(\bar{M}\gamma^2s^2 + \bar{B}_{yy}\gamma s + \bar{K}_{yy}\right) \end{bmatrix} \begin{bmatrix} \bar{X} \\ \bar{Y} \end{bmatrix} = \begin{bmatrix} 0 \\ 0 \end{bmatrix} \tag{33}$$

is obtained. The non-trivial solution of Eq. (33) requires the determinant of the matrix to be zero. The stability requirements for the fluctuations are that the amplitudes of the fluctuations decay with time. This requires $c_\beta \leq 0$. Therefore, the neutral or critical stability solution requires that $s = \pm\hat{j}$ (purely imaginary). Putting these values of s in Eq. (33) and assuming the determinant to be zero provides the solution for critical inertial force $\bar{M}\gamma_c^2$ and critical whirl ratio γ_c as

$$\bar{M}\gamma_c^2 = \frac{\left(\bar{K}_{xx}\bar{B}_{yy} + \bar{K}_{yy}\bar{B}_{xx} - \bar{K}_{xy}\bar{B}_{yx} - \bar{K}_{yx}\bar{B}_{xy}\right)}{\bar{B}_{xx} + \bar{B}_{yy}} \tag{34}$$

$$\text{and } \gamma_c^2 = \frac{\left(\bar{M}\gamma_c^2 - \bar{K}_{xx}\right)\left(\bar{M}\gamma_c^2 - \bar{K}_{yy}\right) - \bar{K}_{xy}\bar{K}_{yx}}{\bar{B}_{xx}\bar{B}_{yy} - \bar{B}_{xy}\bar{B}_{yx}}. \tag{35}$$

The critical inertial force $\bar{M}\gamma_c^2$ represents the impedance to self-excited vibrations. The stability criterion requires that

$$\bar{M}\gamma^2 \leq \bar{M}\gamma_c^2, \tag{36}$$

$$\gamma^2 \leq \gamma_c^2 \tag{37}$$

$$\text{and } \gamma_c^2 \geq 0. \tag{38}$$

4. Numerical methods

Numerical simulations using the Reynolds equation and stability analysis were performed, for which the finite-volume method was employed. The cylindrical domain around the rotor is divided into finite-size area segments. An integration of the Reynolds equation is given as

$$\int_V \nabla\cdot\left[\left(\bar{h}^3\frac{\partial\bar{P}^2}{\partial\theta} - 2\Lambda\bar{P}\bar{h}\right) \quad \frac{\bar{h}^3}{4\lambda^2}\frac{\partial\bar{P}^2}{\partial\bar{z}}\right]^T \mathrm{d}V = -\int_V S_r\mathrm{d}V, \tag{39}$$

which after use of Gauss divergence theorem becomes

$$\int_{\partial V}\left[\left(\bar{h}^3\frac{\partial\bar{P}^2}{\partial\theta} - 2\Lambda\bar{P}\bar{h}\right) \quad \frac{\bar{h}^3}{4\lambda^2}\frac{\partial\bar{P}^2}{\partial\bar{z}}\right]^T\cdot\mathrm{d}\vec{A} = -\int_V S_r\mathrm{d}V. \tag{40}$$

Here S_r represents the relevant source term in the Reynolds Eqs. (13) and (17). Fig. 3 depicts the simple square grid discretization employed. With this discretization, Eq. (40) can be reformulated as

$$\begin{aligned}&\left[\left(\bar{h}^3\frac{\partial\bar{P}^2}{\partial\theta} - 2\Lambda\bar{P}\bar{h}\right)\Big|_E - \left(\bar{h}^3\frac{\partial\bar{P}^2}{\partial\theta} - 2\Lambda\bar{P}\bar{h}\right)\Big|_W\right] \\ &\times\triangle\bar{z} + \left[\left(\frac{\bar{h}^3}{4\lambda^2}\frac{\partial\bar{P}^2}{\partial\bar{z}}\right)\Big|_N - \left(\frac{\bar{h}^3}{4\lambda^2}\frac{\partial\bar{P}^2}{\partial\bar{z}}\right)\Big|_S\right]\triangle\theta = -S_r\triangle\theta\triangle\bar{z},\end{aligned} \tag{41}$$

where $(\cdot)\big|_{E/W/N/S}$ denotes special values of the center of eastern, western, northern or southern faces, respectively. The central difference scheme is used for derivatives of $\bar{P}^2$ along the faces. The central red node, as depicted in Fig. 3, stores the pressure and thickness values ($\bar{P}$, $\bar{h}$). This collocated arrangement requires face values in E, W, N and S faces to be calculated, which are constructed as averages of the neighbors. The nonlinear system of the Eqs. (41) for all grid nodes is solved using the Newton–Raphson method. The source term S_r is linearly dependent on local fluid pressure (18) and therefore can

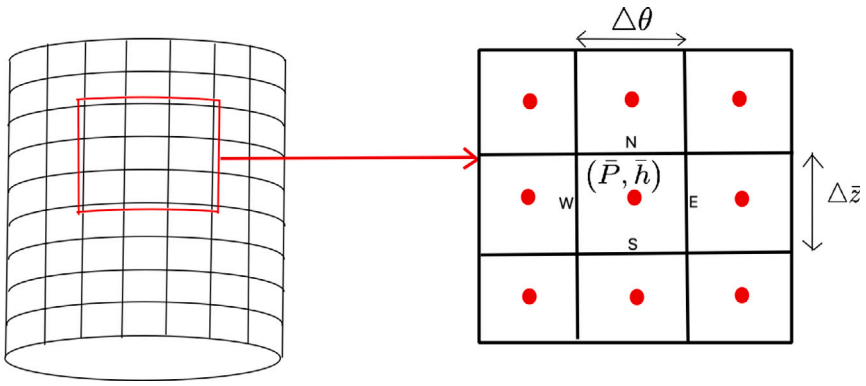

Fig. 3. Figure depicts the grid discretization and data storage points for rotor surface in the numerical simulation.

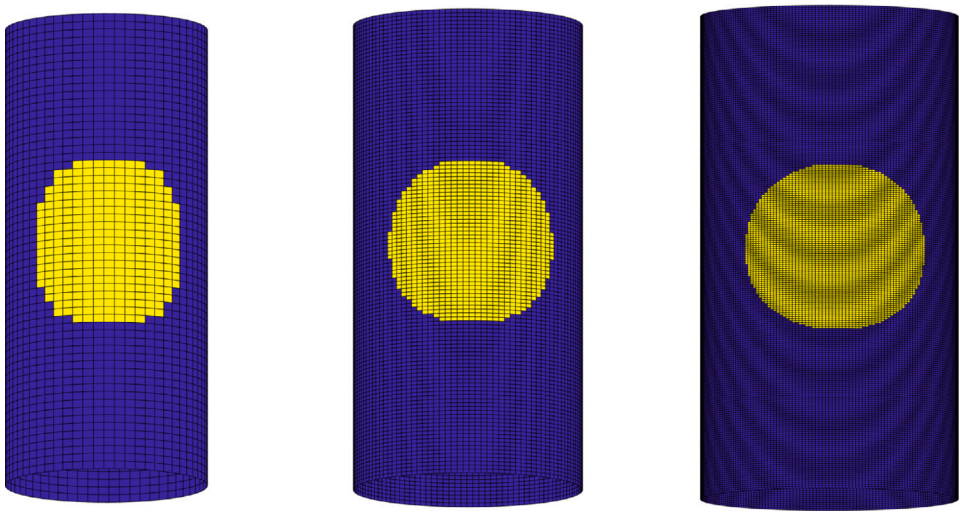

Fig. 4. The figure demonstrates the meshing around the nozzles for number of grid nodes 60,120 and 240 in each of $\bar{z}$ and θ direction. (For interpretation of the references to color in this figure legend, the reader is referred to the web version of this article.)

simply be modeled as function of pressure values at each grid node. The geometrical shape of large nozzle hole is simply approximated using square mesh as demonstrated in Fig. 4. The yellow region in this figure represents the approximation of a circular nozzle geometry on the bearing surface. The Fig. 5 depicts the grid converged solutions for grid nodes $N = 60, 120, 240$ in each of $\bar{z}$, θ directions. The solutions are obtained for $\varepsilon = 0.15, \Gamma_0 = 20, \lambda = 1.75$ and $(d_n/R_b) = 0.7143$. As demonstrated in the figure, the finite volume method along with iterative algorithm for static equilibrium solutions, described in [24], provides grid converged solutions for the modified Reynolds equation. In the rest of the paper in all the numerical analysis, 240 grid nodes are used in each of $\bar{z}$, θ directions for analysis and optimization of bearing design parameters.

5. Results

The rotor size used in the current MAS application is in the range of 0.5 to 10 mm diameter. The corresponding bearing diameter is only slightly larger than the rotor diameter. The length of the bearing ($\sim$0.7 – 2 mm) is limited by the requirement of the RF-coil, used to generate pulses interacting with the spins as well as picking up the free induction decays from the spin system in response to the pulses. Therefore, the nozzle-entry diameter (d_n) to bearing-diameter (R_b) ratio is large compared to the more commonly described individual bearings where it approaches zero. The following results analyze the static and dynamic solutions for pressure, stiffness, damping, bearing supported load and maximum stable inertial force calculations using finite-volume method described in Section 4. The boundary conditions are ambient non-dimensionalized pressure of $\bar{P} = 1$ at $\bar{z} = 0, 1$ and periodic pressure values ($\bar{P}(\theta = 0, \bar{z}) = \bar{P}(\theta = 2\pi, \bar{z})$).

5.1. Bearing stability analysis

Fig. 6 shows the static equilibrium pressure solutions of the Reynolds equation obtained for an aerostatic bearing using a finite-volume method. The bearing geometric properties used are $\lambda = 2.14$, $(d_n/R_b) = 0.7143$ and $N_r = 5$. The bearing number used is $\Lambda = 1$ and the eccentricity ratio is $\varepsilon_0 = 0.03$. The center column of the figure shows the pressure solution for a large nozzle case, i.e. of Eq. (17), which two nozzle restriction parameter values ($\Gamma_0 = 5, 10$) (Fig. 6(b) and (e)). The dimensionless nozzle inlet pressure used in this simulation is $\bar{P}_s = 5$. The left column depicts pressure solutions for the infinitesimal nozzle case, i.e. of Eq. (13) with $\Gamma_0 \in \{9, 25\}$. The choice of the particular nozzle restriction number for infinitesimal nozzles is such that the total nozzle mass flow difference with respect to the large nozzle case is less than five percent. The comparison of the mass flow rate $\dot{m}_{nd}$ for large nozzles and the infinitesimal case through each of the five nozzles placed at equal angular separation of 72° is given Fig. 6(c) and (f). Here, two cases of $\Gamma_0 \in \{5, 10\}$ for large nozzles are employed. Note that θ_n depicts the angular position of the nozzle. The term $\dot{m}_{nd}$ in the right column of Fig. 6 is defined as

$$\dot{m}_{nd} = \begin{cases} \left(\frac{\Gamma_0 \bar{P}_s \delta}{8\lambda}\right) & \text{for infinitesimal nozzle} \\ \left(\frac{R_b^2}{\pi d_n^2}\right) \int_{\bar{A}_n} \left(\Gamma_0 \bar{P}_s \delta\right) \mathrm{d}\theta \mathrm{d}\bar{z} & \text{for finite sized nozzle,} \end{cases} \tag{42}$$

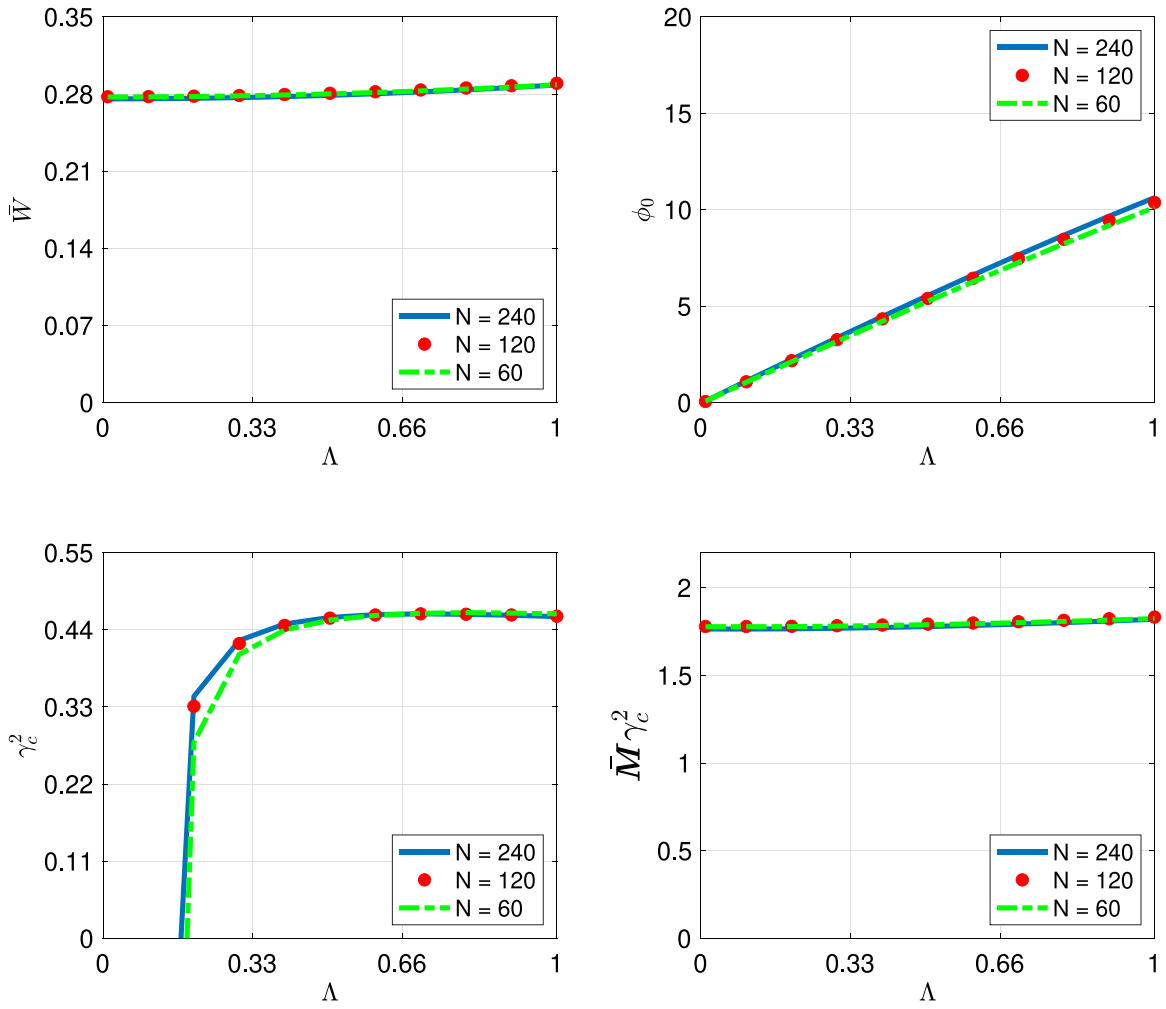

Fig. 5. Grid converging solutions of load ($\bar{W}$), attitude angle (ϕ), critical frequency square (γ_c^2) and critical inertial force ($\bar{M}\gamma_c^2$) using finite volume method.

where $\bar{A}_n$ represents the dimensionless nozzle area scaled by reference $(R_b L)$. Comparison of finite (d_n/R_b) ratio to the infinitesimal nozzle case $(d_n/R_b \rightarrow 0)$ (Fig. 6, left and middle column) shows the effect of resolving the nozzle diameter by the numerical mesh. Infinitesimal nozzle solutions show a concentrated high-pressure peak compared to a distributed nozzle pressure region in the large nozzle case. Therefore, the force calculation cannot be correctly obtained using infinitesimal nozzle approximation for finite value of (d_n/R_b) ratio. This emphasizes the importance of resolving the nozzle size in numerical methods for finite non-zero values of (d_n/R_b). Now it can be computed, by integrating the pressure over the cylindrical rotor surface, the total hydrodynamic force applied to the rotor. The equilibrium attitude angle (ϕ_0) is defined such that total hydrodynamic force contributes only along the load direction $(\bar{y})$ and the total force perpendicular to the load direction $(\bar{x})$ is zero. The static load $(\bar{W})$ and the equilibrium attitude angle (ϕ_0) at different Γ_0 are depicted in the left and center plots of Fig. 7. The static load here represents the total applied force by the bearing to the rotor, which is scaled by $(2P_a L R_b)$. With all other properties (bearing geometry and gas property) kept fixed, varying nozzle restriction number provides an understanding of the role of nozzle diameter to optimize the total applied force provided by the bearing. Under equilibrium conditions, this applied force acts along the $\bar{y}$ direction in Fig. 2. Both load and attitude angle increase with increasing bearing number because the larger bearing number leads to higher fluid speeds at the rotor wall and therefore larger velocity gradients between bearing and rotor wall. Further, an increase in eccentricity leads to increased gradients due to the smaller film thickness sections compared to larger film thickness sections. As a result, the pressure difference between two ends rises. This contributes to enhancement of the net force along the ϵ and ϕ directions due to increased pressure difference. For a fixed speed of rotation, larger rotor mass requires an increase in ϵ_0 to exert more force along the load axis, which leads to an increase in ϕ_0 to balance the forces perpendicular to the load axis.

Fig. 8 shows the dynamic pressure perturbation components (real and imaginary parts of $\bar{P}_\epsilon$ and $\bar{P}_\phi$) for large nozzles with aerostatic bearing parameters $\Gamma_0 = 10, \lambda = 2.14, (d_n/R_b) = 0.7143$ and $N_r = 5$. Real and imaginary parts of $\bar{P}_\epsilon$ represent the sensitivity of the pressure solution to small changes in ϵ and $\dot{\epsilon}$. Similarly, the real and imaginary parts of $\bar{P}_\phi$ represent the sensitivity of the pressure solution to small changes in ϕ and $\dot{\phi}$; cf. Eq. (21). Integrating these perturbation components of the pressure field along the rotor surface provides the stiffness and damping coefficients according to Eqs. (24) and (25), respectively.

The numerical solutions of stiffness and damping are provided in Figs. 9 and 10. The diagonal components of stiffness $\bar{K}_{xx}$ increase weakly with bearing number compared to the off-diagonal component $\bar{K}_{xy}$. The diagonal components of damping $\bar{B}_{xx}$ vary strongly with bearing number compared to the diagonal stiffness components. As a result, the critical inertial force $(\bar{M}\gamma_c^2)$, obtained in the right plot of Fig. 7, increases only weakly with bearing number. This, therefore, limits the maximum stable inertial force with increasing bearing number (frequency of rotation). As a result, the bearing performance in terms of stability is limited by increasing frequency of rotation. Further, the diagonal components of stiffness increases for a fixed value of the bearing number with decreasing nozzle number (Γ_0) as obtained in the

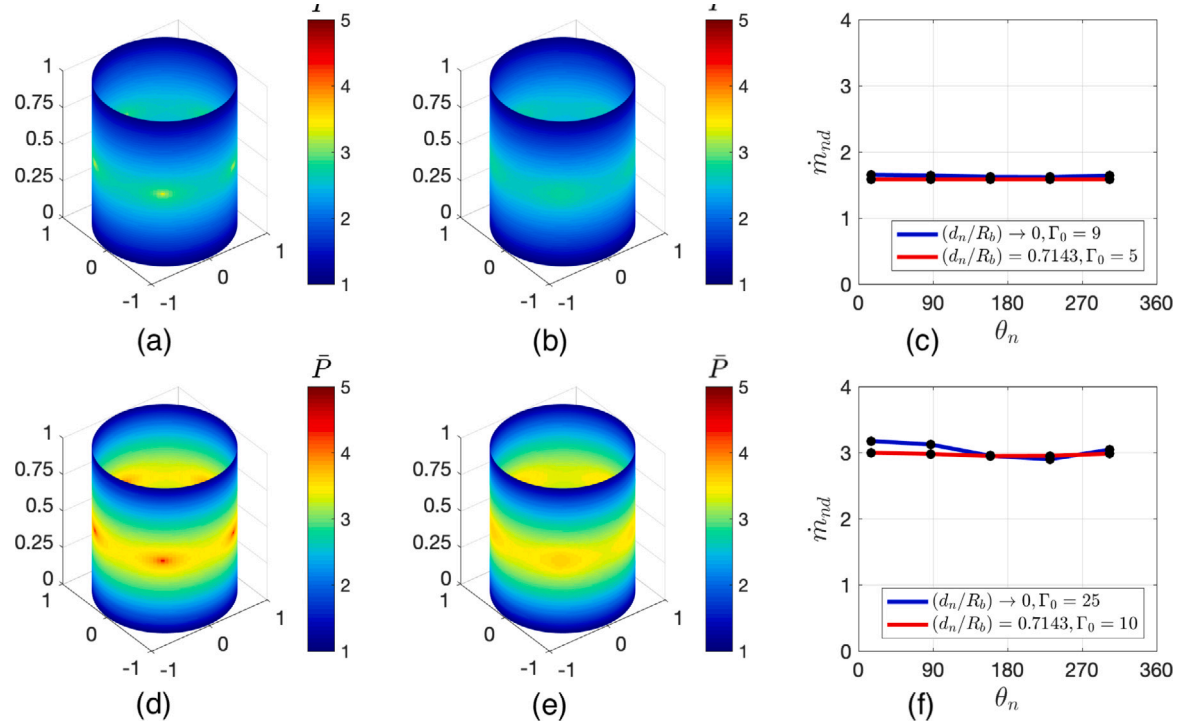

Fig. 6. Comparison of simulation results for dimensionless pressure solutions ($\bar{P}$) around the rotor for an infinitesimal nozzle case ($d_n/R_b \to 0$) and a large nozzle case in the left and center column, respectively. Figure (a) and figure (d) depict the dimensionless pressure solutions for infinitesimal nozzles ($d_n/R_b \to 0$) with $\Gamma_0 = 9$ and 25, respectively. Figure (b) and figure (e) depict the dimensionless pressure solutions for (d_n/R_b) = 0.7143 using $\Gamma_0 = 5$ and 10, respectively. Figure (c) and figure (f) presents the comparisons of dimensionless mass flow rate $\dot{m}_{nd}$ (defined in Eq. (42)) through each nozzle for the large and infinitesimal nozzle cases. The bearing number, eccentricity ratio, aspect ratio and number of nozzles used in this simulation are $\Lambda = 1$, $\varepsilon_0 = 0.03$, $\lambda = 2.14$ and $N_r = 5$, respectively.

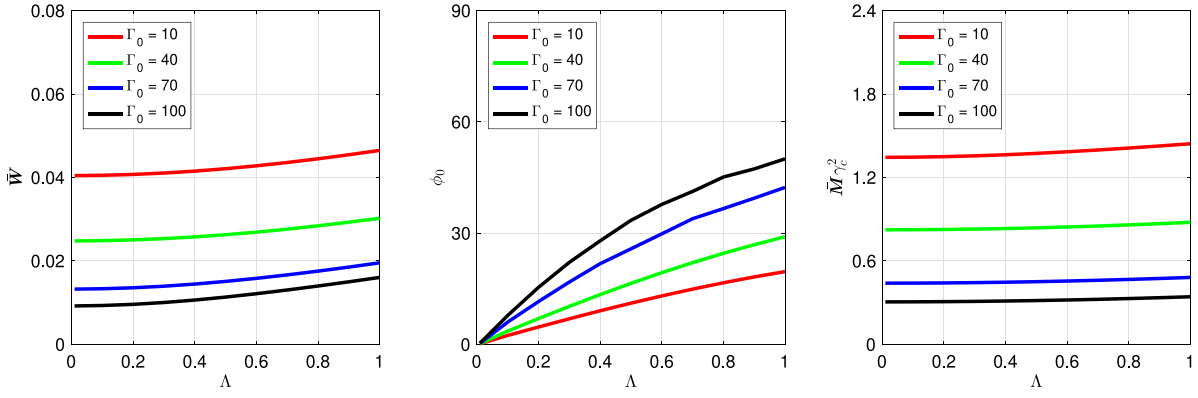

Fig. 7. Static solutions $(\bar{W}, \phi)$ and dynamic solutions $(\bar{M}\gamma_c^2)$ for varying Λ with different values of $\Gamma_0 \in \{10, 40, 70, 100\}$ using $\varepsilon_0 = 0.03, N_r = 5, \lambda = 2.14$ and $(d_n/R_b) = 0.7143$. The figure shows that both load and attitude angle increase with increasing bearing number.

left plot of Fig. 9. Therefore, the nozzle restriction parameter can be optimized to obtain better bearing performance in terms of stability. This further provides an understanding of the role of nozzle diameter in stabilizing the rotor–bearing system. Further investigations of the effect of Γ_0 on the critical inertial force estimation are discussed in the following subsection.

5.2. Comparison of bearing with varying nozzle-diameter to bearing-radius ratio

This subsection is focused on the large nozzle case. As given in Fig. 6, the static equilibrium pressure solution varies significantly for infinitesimal ($d_n/R_b \to 0$) and finite nozzle ($d_n/R_b \sim 1$) cases. This figure shows that for infinitesimal nozzle cases the pressure distributions is more focused near the nozzle entry region. In contrast, the nozzle size effect leads to a more spread out pressure distribution for large nozzle. This therefore leads to different solutions of static load and critical inertial force for varying nozzle restriction numbers. In the remaining part of this subsection, the dependence of bearing characteristics ($\bar{W}, \bar{M}\gamma_c^2$) on nozzle restriction parameter (Γ_0) is analyzed. Fig. 11 depicts the dependence of static and dynamic solutions on nozzle restriction number Γ_0 for different values of nozzle diameter to bearing radius ratio (d_n/R_b). The solutions are given for $\Lambda = 0.5$, $\varepsilon_0 = 0.03$, $\lambda = 2.14$ and $N_r = 5$. For a constant bearing number and eccentricity ratio, the static load $\bar{W}$ and dynamic critical inertial force $\bar{M}\gamma_c^2$ achieve maxima for varying nozzle restriction number. This observation is also true for varying nozzle diameter if the bearing geometry is kept constant. The goal of geometric optimization is to choose the nozzle diameter d_n such that the maximum $\bar{M}\gamma_c^2$ can be achieved. For small Γ_0 values, the variables $\bar{W}$ and $\bar{M}\gamma_c^2$ increases faster with increasing Γ_0. The nozzle restriction number (Γ_0) corresponding to a maximum value of $\bar{M}\gamma_c^2$ increases with increasing (d_n/R_b) ratio. This

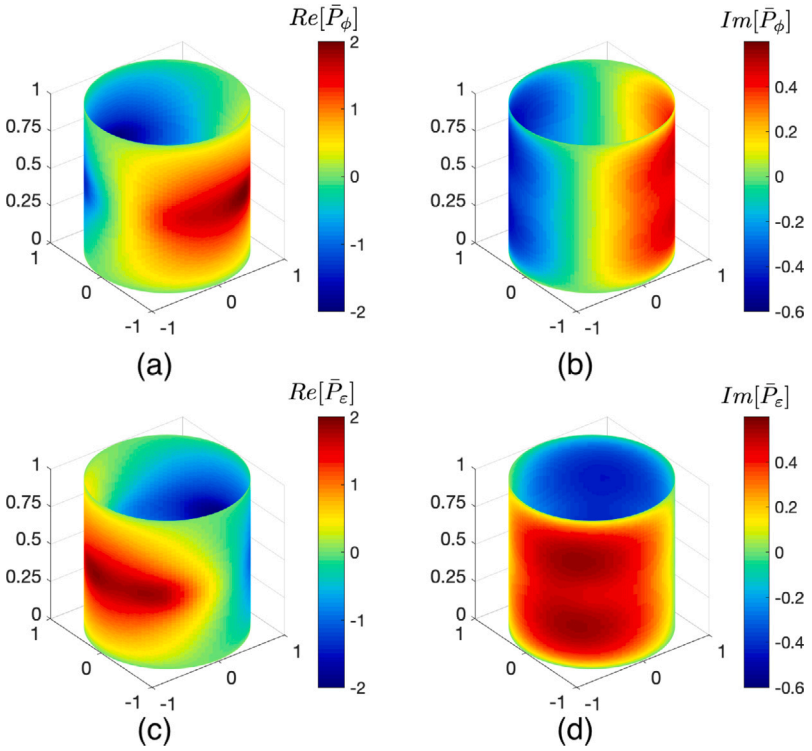

Fig. 8. The real and imaginary parts of the dynamic pressure components $\bar{P}_\varepsilon$ and $\bar{P}_\phi$ for $\Gamma_0 = 10$, $\Lambda = 1$, $\varepsilon_0 = 0.03$, $N_r = 5$ and $\lambda = 2.14$. The real parts are denoted by $Re[\bar{P}_\varepsilon]$ and $Re[\bar{P}_\phi]$. The imaginary parts are denoted by $Im[\bar{P}_\varepsilon]$ and $Im[\bar{P}_\phi]$. The figure obtains the sensitivity of pressure solutions for small perturbation in eccentricity (ϵ) or time derivative of eccentricity ($\dot{\epsilon}$).

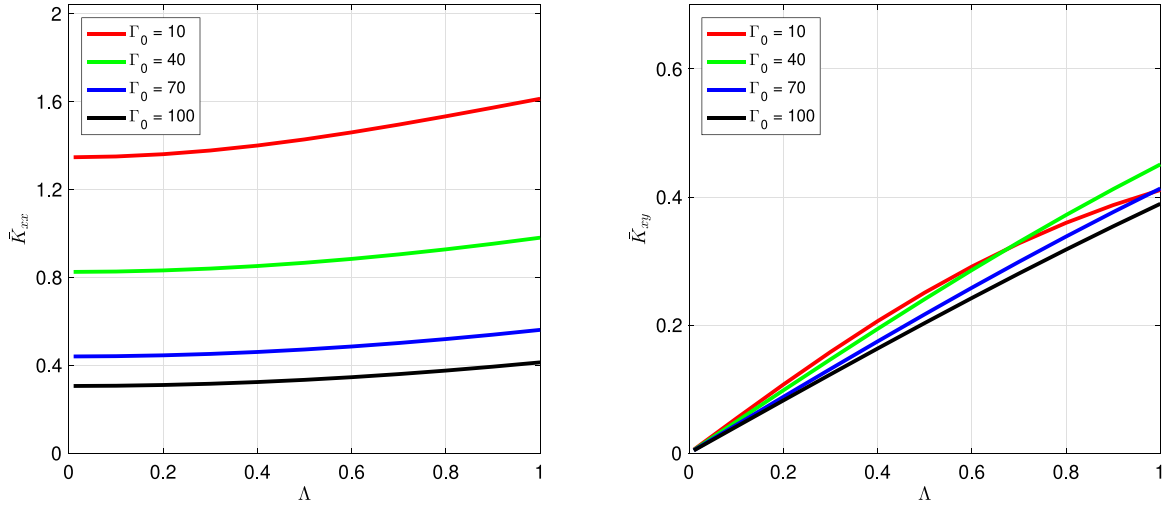

Fig. 9. Stiffness solutions varying with bearing number Λ at different values of $\Gamma_0 \in \{10, 40, 70, 100\}$ using $N_r = 5$, $\varepsilon_0 = 0.03$, $\lambda = 2.14$ and $(d_n/R_b) = 0.7143$.

indicates that the nozzle diameter corresponding to maximum stable inertial force increases with increase in (d_n/R_b) ratio. The maximum values of $\bar{W}$ and $\bar{M}\gamma_c^2$ increase with increasing in (d_n/R_b) ratio. Further increase in Γ_0 from the point corresponding to the maximum $\bar{M}\gamma_c^2$ leads to a decrease in load and critical inertial force solutions at a slower rate and converges to a constant value for large Γ_0. In order to design the bearing to maximize the rotation speed, the choice of small value of Γ_0 near the optimum point is favorable. However, the sharp decay of critical inertial force for smaller Γ_0 leads to higher sensitivity to manufacturing tolerances of the bearing design. Therefore, the effect of manufacturing errors and the optimized design can be minimized by approaching the maximum point of the nozzle restriction parameter from the direction of larger Γ_0.

5.3. Effect of number of nozzles

In this subsection, the impact of number of bearing nozzles on the bearing characteristics is investigated. Fig. 12 provides the solutions of load and critical inertial force with varying nozzle restriction numbers for different values of number of nozzles (N_r). The solutions are obtained for $\Lambda = 0.5$, $\lambda = 2.14$, $(d_n/R_b) = 0.4762$ and $\varepsilon_0 = 0.03$. The maximum values of $\bar{W}$ and $\bar{M}\gamma_c^2$ decrease with increasing nozzle restriction number as presented in the right plot of Fig. 12. Furthermore, the maximum value of critical inertial force increases with increasing numbers of nozzles. However, since the peak value location of Γ_0 shifts towards lower values with increasing nozzle number, the enhancement of stability performance with changing N_r depends very much on the

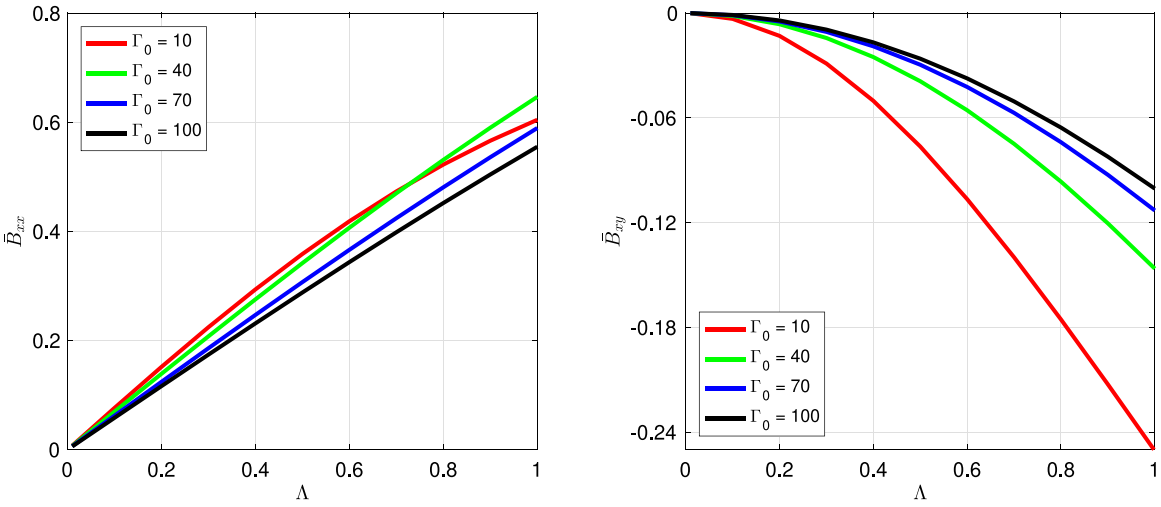

Fig. 10. Damping solutions varying with bearing number Λ at different values of $\Gamma_0 \in \{10, 40, 70, 100\}$ using $N_r = 5$, $\epsilon_0 = 0.03$, $\lambda = 2.14$ and $(d_n/R_b) = 0.7143$.

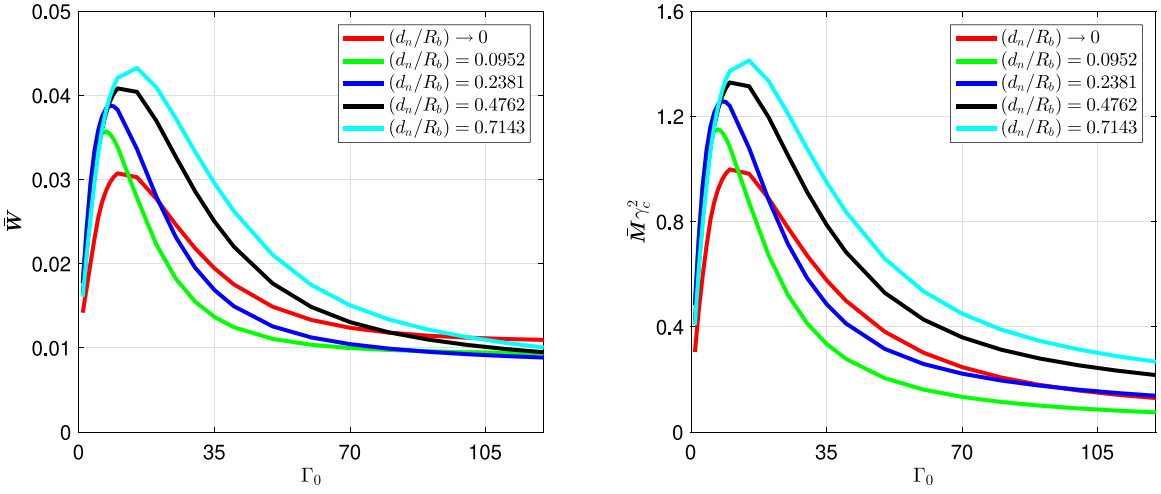

Fig. 11. Static and dynamic solutions for varying nozzle restriction number Γ_0 with different nozzle diameter to bearing radius ratios. There exists an optimum value of Γ_0, which leads to maximum stable critical inertial force $(\bar{M}\gamma_c^2)$.

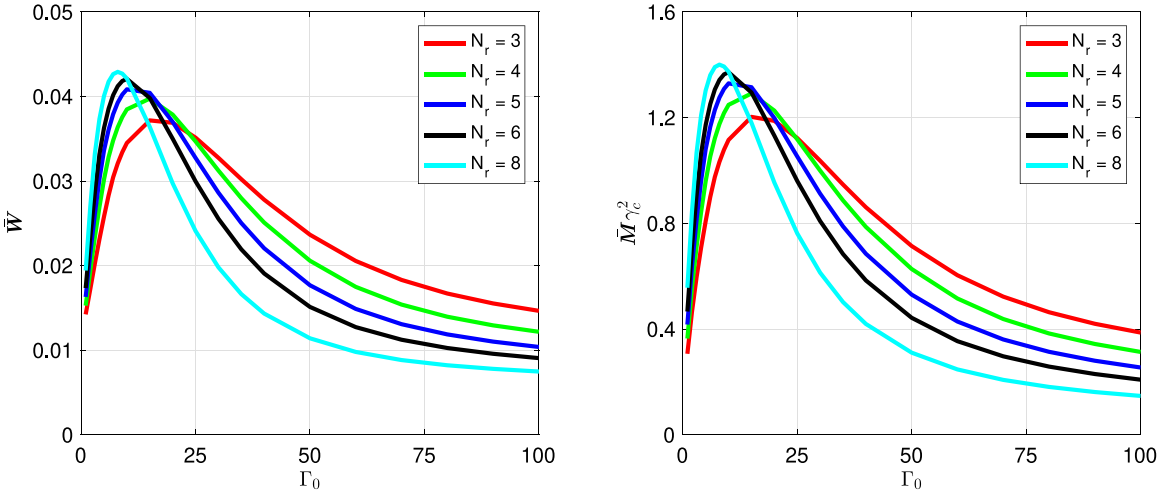

Fig. 12. Figure shows the static and dynamic solutions for varying nozzle restriction number Γ_0 at different values of number of nozzles (N_r). The maximum balancing weight and maximum critical inertial force increases with increase in number of nozzles (N_r). However, the optimum nozzle diameter size decreases with increasing number of nozzles.

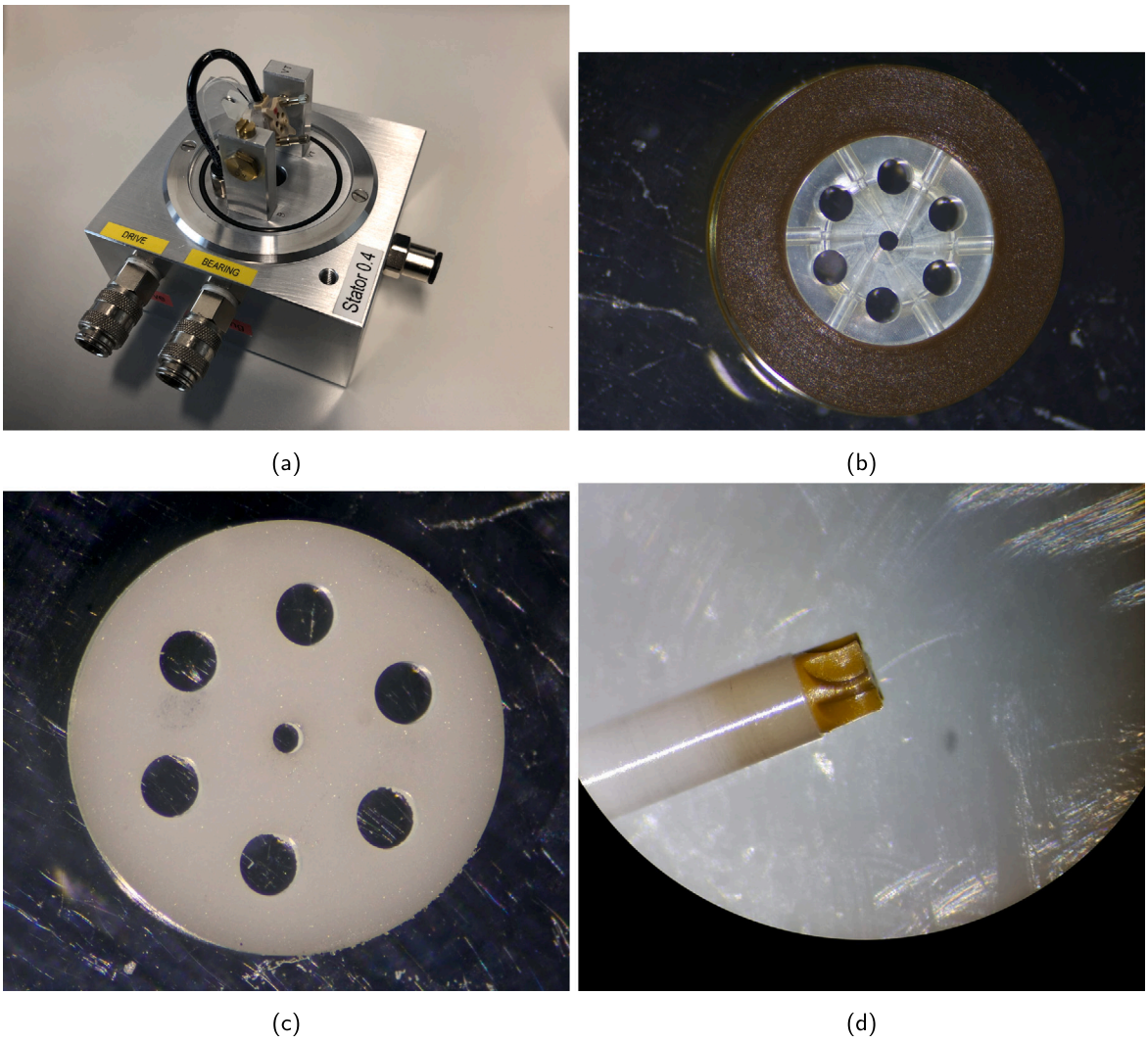

Fig. 13. Four components of the experimental setup. Figure (a) shows the full setup of rotor and stator. Figure (b) depicts the nozzle entry to the turbine. Figures (c) and (d) respectively provide images of bearing and the turbine blades of the rotor.

operating point for Γ_0. Furthermore, the effect of more than five nozzles is relatively small.

5.4. Comparison of bearing design

5.4.1. Experimental set-up

The Fig. 13 provides images of different components of the rotor–turbine–bearing system, which is used in the experiment for comparison of bearing design. The part (a) of the figure portrays the entire setup of rotor and stator. Two gas-flow streams provide the required high pressure for turbine (drive) and bearing as mentioned in the figure. The drive gas-flow stream goes through six nozzles illustrated in the part (b) of the figure, which are used to provide high-pressure gas feed to rotate the turbine. The part (c) of the figure illustrates the image of a bearing with six nozzles. The nozzles, which are not visible here, are placed between each pair of the six holes located concentrically from bearing center. The rotor has the turbine in front, which is further microscopically visualized in the part (d) of the figure. A dark mark is placed in back end of the rotor, which is detected via optical sensors placed in the stator. An oscilloscope is used to convert these measurements into frequency calculation. Following steps describe the experiment to test the bearing performance.

1. At first, the high-pressure gas stream is provided via bearing entry into the experimental setup.
2. After fixing bearing pressure to a particular value, the drive entry is provided with high pressure stream. The pressure is increased while observing oscilloscope frequency calculation. The oscilloscope provides an average frequency value and standard deviation of the frequency value. A target frequency value is set in the oscilloscope and drive pressure is increased until this target value is reached, while keeping the standard deviation minimized (<20 Hz). The corresponding drive pressure, bearing pressure and the measured frequency are noted.
3. Step two is repeated until any instability is observed in the oscilloscope frequency calculation. This instability is indicated in oscilloscope by large standard deviation in the observed average frequency (>1 kHz). At this point, the bearing pressure is increased to a higher value unless the observed instability disappears.
4. The steps two and three are repeated until it is impossible to increase the rotation frequency by enhancing the drive pressure.

Fig. 14a portrays the internal part of the experimental setup, which is sketched in Fig. 13a. The cross-section of the aerostatic bearing used to stabilize the rotor is displayed in Fig. 14b. The details of the experimental results with different bearing types are reported and discussed in the following sub-section.

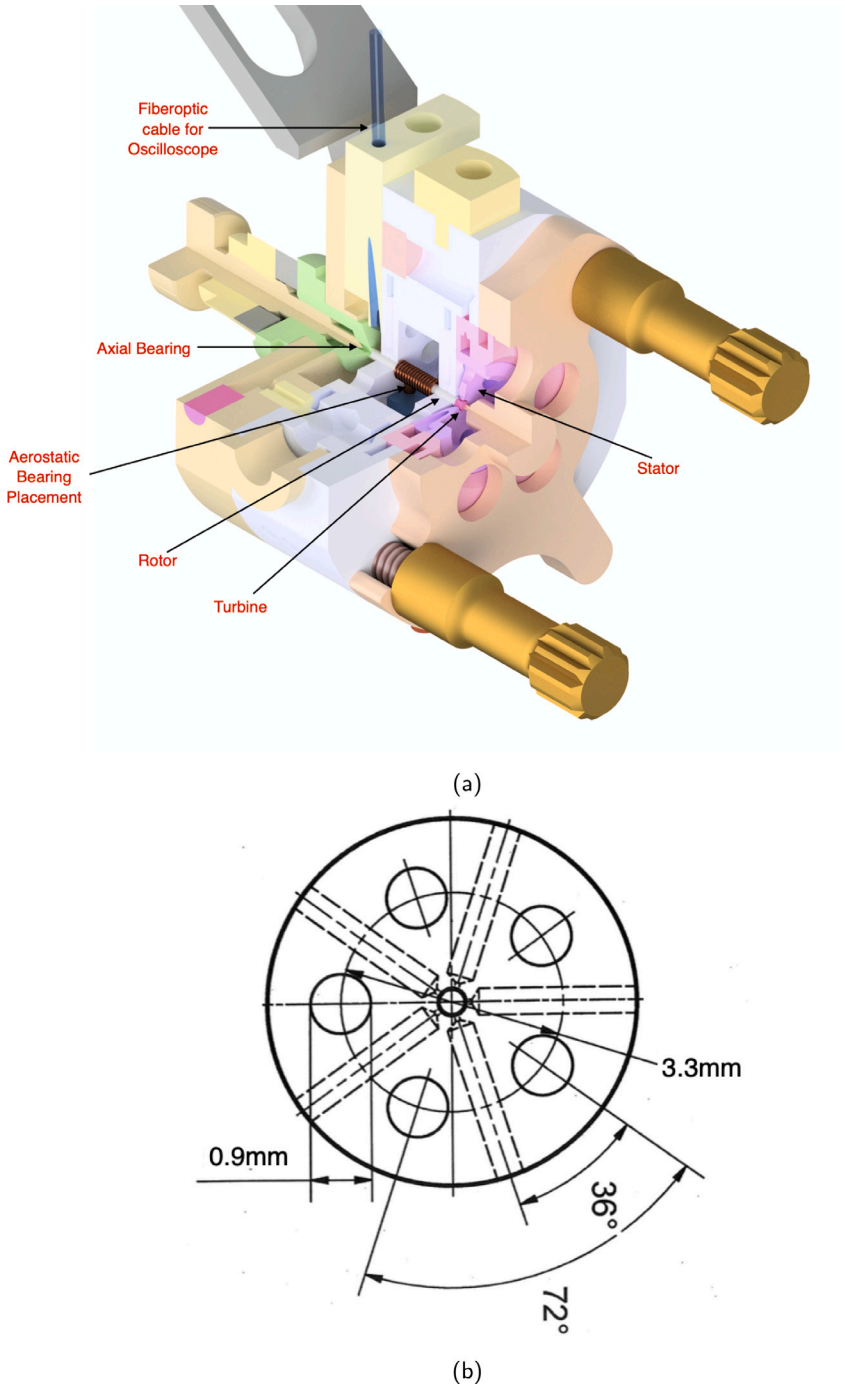

Fig. 14. Top: 3D sketch of experimental setup. Bottom: the internal cross-section of a bearing.

5.4.2. Comparison of experiments with numerical results

In this section, a commercially available bearing denoted as Be_2 is compared with in house development of three different bearing types denoted as Be_1, Be_3 and Be_4. The geometric design parameters and essential non-dimensional numbers for different bearing configurations are summarized in Tables 1 and 2. The Fig. 13 provides the details of the experimental setup used to test different bearings. The term $\bar{W}_r$ in Tables 1 and 2 denotes the non-dimensionalized rotor weight stabilized by each bearing along the direction perpendicular to the axis of bearing. For a given rotor weight m_r, magic-angle $\theta_{MAS} = 54.74°$ and acceleration due to gravity g, the term $\bar{W}_r$ is given as

$$\bar{W}_r = \left(\frac{0.5 m_r g \sin\theta_{MAS}}{2 P_a L R_b} \right). \tag{43}$$

The factor 0.5 in Eq. (43) is introduced due to the use of two bearings in the present configuration cf. 1 to balance the total weight component perpendicular to rotor axis. The commercial bearing system is significantly larger than other bearing systems ($R_b = 0.675$ for Be_2, $R_b = 0.21$ for $Be_{1,3,4}$). However the performance of Be_1 in terms of maximum stable rotational frequency (f_{max}) was only 25 kHz compared to 70 kHz for Be_2. This large reduction in f_{max} is explained by calculating the critical inertial force ($\bar{M}\gamma_c^2$) as a function of nozzle restriction parameter

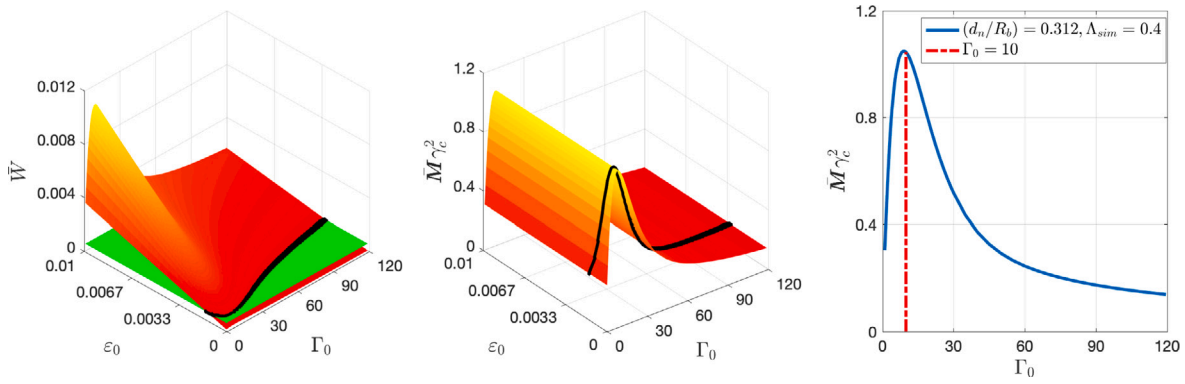

Fig. 15. $2D$ spline interpolation of static and dynamic solutions with varying $(\Gamma_0,\ \varepsilon_0)$ for bearing type Be_2. The black curves in the left and central figures represent the intersection of the $3D$ surface with the rotor non-dimensional weight solution $(\bar{W})$. The central plot shows the maximum stable inertial force solution $\bar{M}\gamma_c^2$ for varying ε_0 and Γ_0. Finally, in the right plot $\bar{M}\gamma_c^2$ is plotted against Γ_0 along the intersection curve presented in the left and central figures. The design point (Γ_0) of the nozzle used in the experiment for Be_2 is located very close to the optimum nozzle restriction number as represented by the dashed red line in the right plot. (For interpretation of the references to color in this figure legend, the reader is referred to the web version of this article.)

Table 1
Coefficients of bearing types Be_1, Be_2, Be_3 and Be_4.

Variable notation	Be_1	Be_2	$Be_3(T_1)$	$Be_3(T_2)$	Be_3, Helium	Be_4
c (mm)	0.0075	0.023	0.01	0.01	0.01	0.01
C_d	0.7	0.7	0.7	0.7	0.7	0.7
d_n (mm)	0.15	0.21	0.1	0.1	0.1	0.15
D_r (mm)	0.4	1.3	0.4	0.4	0.4	0.4
f_{max} (kHz)	25	70	110	85	25	18
L (mm)	0.7	1.8	0.9	0.9	0.9	0.9
m_r (mg)	1.9	32.2	1.9	1.9	1.9	1.9
R_b (mm)	0.2075	0.673	0.21	0.21	0.21	0.21
R^0 (J/kg/K)	288.68	288.68	288.68	288.68	1099.3	288.68
T^0 (K)	298	298	298	298	298	298
(d_n/R_b)	0.7229	0.312	0.4762	0.4762	0.4762	0.714
N_r	5	5	5	6	5	5
$\bar{W}_r$	2.59×10^{-4}	5.25×10^{-4}	1.99×10^{-4}	1.99×10^{-4}	1.99×10^{-4}	1.99×10^{-4}
κ	1.4	1.4	1.4	1.4	1.66	1.4
Γ_0	147	9	27	27	108	60
Λ_{max}	0.12	0.38	0.3	0.25	0.05	0.07
Λ_{sim}	0.1	0.4	0.3	0.2	0.1	0.1
λ	1.69	1.34	2.14	2.14	2.14	2.14

Table 2
Coefficients of bearing types Be_5, Be_6 and Be_7.

Variable notation	Be_5	Be_6	Be_7
c (mm)	0.012	0.015	0.023
C_d	0.7	0.7	0.7
d_n (mm)	0.1	0.1	0.21
D_r (mm)	0.4	0.4	3.2
f_{max} (kHz)	110	95	22
L (mm)	0.9	0.9	1.7
m_r (mg)	1.9	1.9	253
R_b (mm)	0.21	0.21	1.623
R^0 (J/kg/K)	288.68	288.68	288.68
T^0 (K)	298	298	298
(d_n/R_b)	0.4762	0.4762	0.129
N_r	5	5	6
$\bar{W}_r$	1.66×10^{-4}	1.33×10^{-4}	1.82×10^{-3}
κ	1.4	1.4	1.4
Γ_0	16	8	10
Λ_{max}	0.208	0.133	0.71
Λ_{sim}	0.2	0.1	0.7
λ	2.14	2.14	0.52

(Γ_0) for Be_1 and Be_2. A direct comparison of the stability plot for a constant equilibrium eccentricity ratio (ε_0), as obtained in Fig. 11 is not appropriate in the cases of Be_1 and Be_2 with varying bearing geometries. Also, the non-dimensional rotor weight $\bar{W}_r$ is fixed in both cases of the bearings Be_1 and Be_2. The procedure for obtaining the critical quantities as a function of Γ_0 is shown in the algorithm 1. The left of Fig. 15 shows the calculated load $\bar{W}$ as a function of ε_0 and Γ_0 for a fixed bearing number Λ. The fixed bearing number was chosen based on the maximum frequency of rotation f_{max} as given in the Tables 1 and 2. Using the bearing geometry parameters and f_{max}, the maximum bearing number Λ_{max} was calculated and is reported in the Tables 1 and 2. The term Λ_{sim} was calculated as a multiplier of 0.1, which is numerically nearest to Λ_{max}. Furthermore, the constant green plane defines the rotor weight $\bar{W}_r$ as given in Eq. (43), which is constant with respect to ε_0 and Γ_0. The black curve in this plot represents the intersection of constant $\bar{W}_r$ where $\bar{W}(\varepsilon, \Gamma_0)$ was obtained numerically. Physically, this curve represents the variation of ε_0 with changing Γ_0 such that the balanced weight $\bar{W}$ is equal to $\bar{W}_r$. The center plot shows the critical inertial force plotted as a function of ε_0 and Γ_0. Furthermore, the corresponding value of critical inertial force for $\bar{W} = \bar{W}_r$ is marked as black curve in this figure. Finally, in the right figure, the value of critical inertial force is plotted against Γ_0 along the $\bar{W} = \bar{W}_r$ curve. The dashed red line in the right figure represents the numerical value of critical inertial force corresponding to the experimental Γ_0 value for Be_2. The plot clearly shows that the design of Be_2 works right at the optimum value of Γ_0. Similarly, the $\bar{M}\gamma_c^2$ vs. Γ_0 curve for constant non-dimensional rotor weight is given for bearing types Be_1 and Be_3 in Figs. 16 and 17, respectively. The top plot (a) of Fig. 19 provides the comparison of the $\bar{M}\gamma_c^2$ vs. Γ_0 plots for bearing types Be_1 and Be_2. It is apparent from Fig. 16 that the nozzle restriction parameter $(\Gamma_0 = 147, \bar{M}\gamma_c^2 = 0.125)$ is not optimized in Be_1 compared to design Be_2 $(\Gamma_0 = 10, \bar{M}\gamma_c^2 = 1.04)$. Such stability plots are used to optimize Γ_0 in order to enhance the critical inertial force with the goal of increasing stable rotational frequency. Fig. 18 depicts the solutions of the squared critical whirl ratio (γ_c^2) with $\bar{W} = \bar{W}_r$ at varying

Algorithm 1: Optimization Algorithm

Using bearing and rotor geometric configuration $(L, R_b, c, \omega_r, d_n)$, rotor mass (m_r) and fluid properties (μ, P_a), estimate dimensionless numbers Λ, λ, Γ_0 and $\bar{W}_r$.
Select a set of values $\{\Gamma_0^1, \Gamma_0^2, \ldots \Gamma_0^n\}$ for nozzle restriction number, such that $\Gamma_0^1 = 1$ and $\Gamma_0 < \Gamma_0^n$.
Set a tolerance value Tol for iterative steps to obtain the attitude angle.
for $i = 1;\ i \leq n; i++$ **do**
  Select a set of values $\{\varepsilon_0^1, \varepsilon_0^2, \ldots \varepsilon_0^m\}$ of equilibrium eccentricity.
  for $j = 1;\ j \leq m; j++$ **do**
    Set $k = 0$ and $\Delta\phi_0 = 0$.
    Set an initial guess for attitude angle as ϕ_0.
    Obtain film thickness field $\bar{h}_0 = 1 + \varepsilon_0^j \cos(\theta - \phi_0)$.
    while $(k == 0)$ *or* $\Delta\phi_0 > Tol$ **do**
      Solve the dimensionless Reynold's equation (17).
      Using a numerical integration, estimate the dimensionless force components $\bar{F}_x^{(i,j)}$ and $\bar{F}_y^{(i,j)}$ applied by the fluid film pressure $\bar{P}$ on the rotor surface.
      Set $\Delta\phi_0 = \tan^{-1}(\bar{F}_x^{(i,j)} / \bar{F}_y^{(i,j)})$.
      Set $\phi_0 = \phi_0 + \Delta\phi_0$.
      Obtain film thickness field $\bar{h}_0 = 1 + \varepsilon_0^j \cos(\theta - \phi_0)$.
      Set $k = k + 1$.
    end
    Estimate the solution for $\bar{F}_y^{(i,j)}$ as a force to balance the dimensionless weight.
    Calculate using linear stability analysis solutions for $\left(\gamma_c^2\right)^{(i,j)}$ and $\left(\bar{M}\gamma_c^2\right)^{(i,j)}$.
  end
end
Obtain solution for dimensionless weight $\bar{W}$ using suitable interpolation scheme and the dataset $(\Gamma_0^i, \varepsilon_0^j, \bar{F}_z^{(i,j)})$.
Obtain solution for inertial force $\bar{M}\gamma_c^2$ using suitable interpolation scheme and the dataset $\left(\Gamma_0^i, \varepsilon_0^j, \left(\bar{M}\gamma_c^2\right)^{(i,j)}\right)$.
Estimate the set of points for $(\varepsilon_0, \Gamma_0)$ such that $\bar{W} = \bar{W}_r$. This set of points is denoted as $(\varepsilon_0, \Gamma_0)|_{\bar{W}=\bar{W}_r}$.
Find $\bar{M}\gamma_c^2$ for the points $(\varepsilon_0, \Gamma_0)|_{\bar{W}=\bar{W}_r}$.
Find the value of Γ_0^{opt} such that $\bar{M}\gamma_c^2$ is maximized.
Find optimized diameter $d_n^{opt} = d_n \sqrt{\left(\Gamma_0^{opt} / \Gamma_0\right)}$.

nozzle restriction numbers for the three bearing types Be_1, Be_2 and Be_3. The numerical values of γ_c^2 converge towards 0.5 for all three bearing types. The numerical results show a weak dependence of whirl ratio on nozzle restriction number and therefore on the inertia imparted due to air flow through the nozzle.

As a next step, the bearing design Be_1 is optimized by reducing nozzle diameter d_n, increasing clearance c and increasing the bearing length L. This optimized bearing design is denoted as Be_3. Moreover two variants of Be_3 are designed with different numbers of nozzles (N_r). These two variants are denoted as (Be_3, T_1) for $N_r = 5$ and (Be_3, T_2) for $N_r = 6$. The bearing type Be_4 is obtained from Be_1 by increasing c and L only. The number of nozzles used in Be_4 is 5. The $\bar{M}\gamma_c^2$ vs. Γ_0 curve along the constant rotor weight for Be_3 and Be_4 are shown in the bottom plot (b) of Fig. 19. Furthermore, the corresponding experimental points for Γ_0 for (Be_3, T_1), (Be_3, T_2), Be_4 are plotted as dashed lines. The use of diameter $d_n = 0.1$ mm in Be_3 and $d_n = 0.15$ mm in Be_4 along with a clearance of $c = 0.01$ mm lead to nozzle restriction parameter values of 27 and 60, respectively. The numerical calculation of critical inertial force provides $\bar{M}\gamma_c^2 = 0.3$ for (Be_3, T_1) and $\bar{M}\gamma_c^2 = 0.15$ for Be_4. The performance in terms of maximum stable frequency is obtained as $f_{max} = 110$ kHz for $\Gamma_0 = 27$ in (Be_3, T_1) compared to $f_{max} = 25$ kHz for $\Gamma_0 = 60$ in Be_4, which correlates with increasing $\bar{M}\gamma_c^2$. The changes in number of nozzles (N_r) also plays an important role in enhancing the inertial force as represented by the green $(N_r = 6)$ and red $(N_r = 5)$ solid curves in Fig. 19(b). The corresponding value of $\bar{M}\gamma_c^2$ at $\Gamma_0 = 27$ for six nozzles is 0.25 compared to 0.3 for the five nozzles case. This therefore leads to a reduction in maximum stable frequency to 85 kHz for (Be_3, T_2) compared to 110 kHz for (Be_3, T_1). The experimental value of the maximum stable bearing number is plotted against the numerical calculation of critical inertial force in the top right plot (b) of Fig. 20. The solid lines in the top left plot (a) of Fig. 20 give the relation between bearing number and MAS frequency for different geometric configurations of the bearing. The dashed lines here represent the experimentally obtained maximum stable MAS frequency of the corresponding bearing. The green line here correspond to the bearing Be_2, which is an outlier in terms of bearing geometry and rotor size value among the different bearings used. This is due to the large bearing radius for Be_2 compared to $Be_{1,3,4}$. The large bearing radius for Be_2 leads to a maximum slope in Λ vs. f; depicted as the + marker point in plot 20(b). This also confirms that it is an outlier in the current design configuration study. However, the increased stable inertial force in the case of Be_2 also leads to higher stable bearing numbers obtained experimentally. The blue points on the $\bar{M}\gamma_c^2$ vs. Λ plot can be connected via dashed lines represent the increase of the bearing number from Be_4 to (Be_3, T_2) and to (Be_3, T_1) in the top right plot (b) of Fig. 20. All these three bearing geometries lead to the same slope in the frequency-bearing number plot (solid blue line in the top left part (a) of Fig. 20). The $\bar{M}\gamma_c^2$ vs. Λ plot further confirms the strong correlation between increasing stable inertial force and enhanced rotational frequency. In addition to optimizing the nozzle restriction number, the bearing length (L) is also increased in Be_3 and Be_4 compared to Be_1. This leads to a reduction of the non-dimensional rotor weight $(\bar{W}_r)$ in Be_3 and Be_4 compared to Be_1 for the same absolute rotor weight. Another outlier rotor geometry in the top right plot corresponds to the bearing type Be_7 with $D_r = 3.2$ mm. The maximum stable frequency for Be_7 is obtained as 22 kHz. The family of bearing types for rotor diameter $D_r = 0.4$ mm is presented in the bottom left plot (c) of Fig. 20. The bottom right plot shows $\bar{M}\gamma_c^2$ vs. f_{max} for the family of bearing types with rotor diameter $D_r = 0.4$ mm. Finally, it can be concluded based on these numerical calculations and experimental results that in order to achieve maximum stable rotational frequency, maximization of stable inertial force $(\bar{M}\gamma_c^2)$ can be used as a design criterion of bearing geometry and nozzle diameter for a fixed rotor size. One way to achieve this maximization of stable inertial force is to choose an optimum nozzle restriction number and therefore nozzle diameter, which can be used as a guide to optimize the bearing design for maximum stable rotational frequency. Due to tolerance issue in creating small nozzle diameter in our manufacturing facility, the investigation with decreasing nozzle diameter could not be achieved. Therefore, a bearing could not be manufacture and its performance could not be reported in terms of maximum rotor frequency, which optimizes the maximum critical inertial force for 0.4 mm rotor. However, it is interesting to observe that commercial bearing type Be_2 is perfectly designed to have optimized maximum critical inertial force as obtained in Fig. 19(a).

The bearing type Be_3 is tested with helium gas feed of the bearing nozzle and compared with air feed. The corresponding nozzle restriction number increases about four times for Helium compared to air feed. This is because of the small molecular weight of helium, which leads to a large specific gas constant per unit mass. The maximum stable frequency experimentally obtained with Helium for bearing type (Be_3, T_1) is 18 kHz compared to 110 kHz with air. This test using helium further confirms the role of the nozzle restriction number in maximizing the stable inertial force, which leads to changes in the maximum rotation frequency. The change in bearing clearance for Be_3

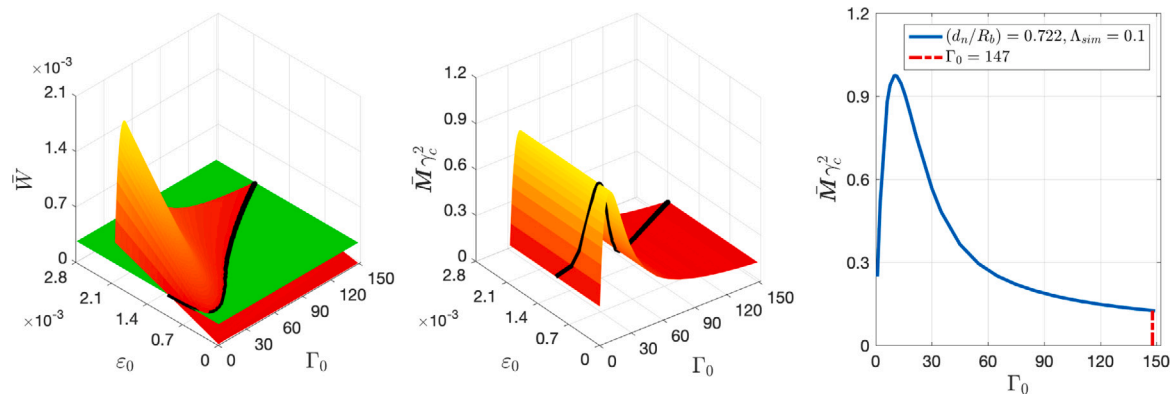

Fig. 16. $2D$ spline interpolation of static and dynamic solutions with varying (Γ_0, ε_0) for bearing type Be_1. The design point (Γ_0) of the nozzle used in the experiment for Be_1 is located far off from the optimum nozzle restriction number as represented by the dashed red line in the right plot. (For interpretation of the references to color in this figure legend, the reader is referred to the web version of this article.)

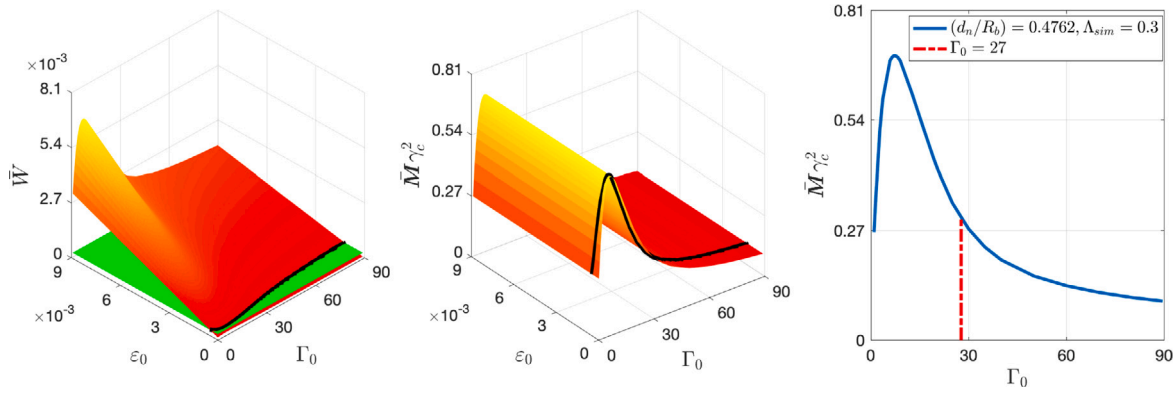

Fig. 17. $2D$ spline interpolation of static and dynamic solutions with varying (Γ_0, ε_0) for bearing type Be_3. The design configuration of the nozzle used in the experiment for Be_3 is improved in terms of enhanced inertial force value corresponding to the experimental nozzle restriction number, while compared with Be_1 used for 0.4 mm rotor.

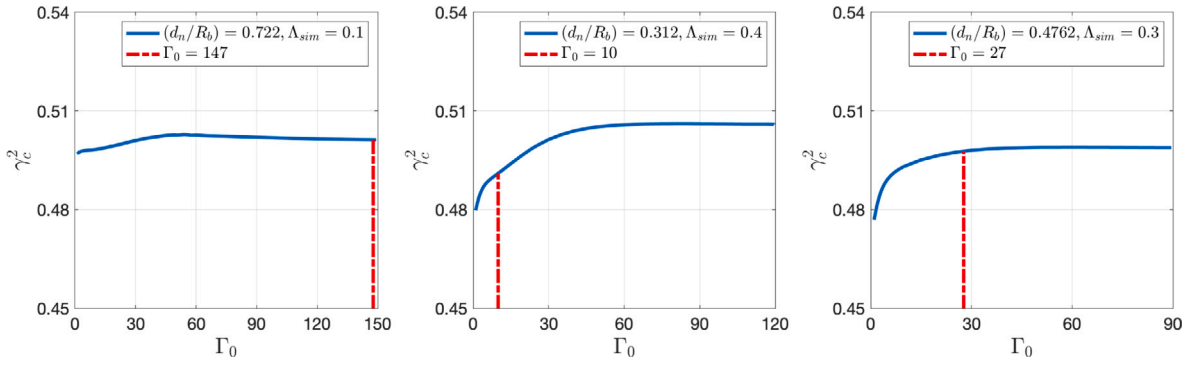

Fig. 18. γ_c^2 is plotted against Γ_0 along the interaction curves depicted for bearing types Be_1, Be_2 and Be_3 respectively from left to right.

is represented by the bearing design Be_5 and Be_6. The clearance values are chosen as $c = 0.012$ mm and $c = 0.015$ mm for Be_5 and Be_6 respectively. An enhancement of rotor frequency could not be achieved beyond 110 kHz for further enhancement of the maximum stable inertia number $(\bar{M}\gamma_c^2)$. This is most likely due to the limitations of torque provided by the airflow around the turbine.

6. Conclusion

The Reynolds equation for aerostatic bearings with infinitesimal nozzle size was modified to account for the effect of finite nozzle diameter to bearing radius ratio. Finite volume based numerical stability analyses were then performed and grid converged solutions of load, attitude angle, critical frequency square and critical inertial force are presented. The large nozzle case was simulated and compared with the infinitesimal nozzle case for varying (d_n/R_b) ratio. It is shown that the optimized nozzle restriction number (Γ_0) and the maximum critical inertial force ($\bar{M}\gamma_c^2$) increase with increasing (d_n/R_b) ratio. Numerical solutions for load and critical inertial force are also presented for varying numbers of nozzles. It is found that the optimal Γ_0 decreases with increasing number of nozzles.

In order to obtain the optimized nozzle restriction number for bearing design, a new calculation strategy is proposed here. In this calculation method, the optimized Γ_0 is obtained along a curve of fixed non-dimensional rotor weight. Based on this optimization procedure, the bearing design to enhance the stable rotor frequency is proposed. The main objective here is to maximize the critical inertial force along the fixed rotor weight curve. Finally, several experimental designs were

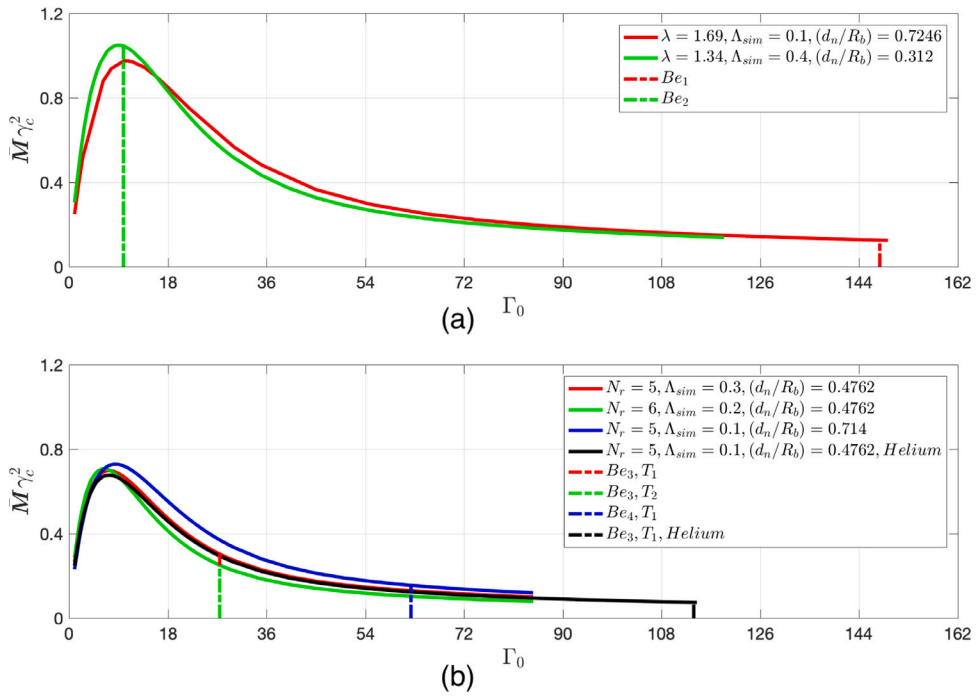

Fig. 19. $\bar{M}\gamma_c^2$ vs. Γ_0 solutions plotted along constant rotor weight curves for bearing types Be_1, Be_2, Be_3 and Be_4. The dashed lines depict the solutions of $\bar{M}\gamma_c^2$ for experimental values of nozzle restriction number Γ_0 for different bearing types. The top plot (*a*) shows $\bar{M}\gamma_c^2$ vs. Γ_0 for bearing type Be_1 and Be_2. The bottom plot (*b*) shows the same for bearing type Be_3 and Be_4 using varying nozzle numbers and varying nozzle flow gas types. (For interpretation of the references to color in this figure legend, the reader is referred to the web version of this article.)

tested for magic-angle spinning (MAS) devices, employing two specific bearing and rotor sizes. New bearing design leads to the enhancement of the rotor frequency from 25 kHz to 110 kHz. Furthermore, the effect of different gases as impinging fluid in the bearing nozzle is also analyzed experimentally by replacing air with Helium. As expected, due to increase in Γ_0 with use of Helium, the performance of bearing to stabilize the rotor frequency decreases significantly.

Based on the experimental observation and supporting numerical investigation, it is recommended to optimize the value of nozzle restriction number in order to maximize the bearing performance. It is concluded that the bearing system has a significant effect on the performance of small MAS rotors. Although the present study concentrates on special bearings for MAS systems, the analysis is valid for a wider range of bearings with finite nozzle to bearing radius ratio. Thus application to other microturbine systems could also be of interest in future studies.

Declaration of competing interest

The authors declare that they have no known competing financial interests or personal relationships that could have appeared to influence the work reported in this paper.

Data availability

Data will be made available on request.

Acknowledgment

The work was supported by an ERC Advanced Grant (B.H.M., grant number 741863, FASTER), and by the Swiss National Science Foundation (B.H.M., grant number 200020_188711).

Appendix A

Fig. 21 depicts the local coordinates for flow in the gap between bearing and rotor. The velocity components u_x and u_z represents the two orthogonal components of flow parallel to the local tangent plane of the rotor wall. The component u_z depicts the flow perpendicular to the rotor velocity into the plane of figure. The coordinate y represents the space variable along the bearing–rotor gap. The Reynolds equation with nozzle entries is derived in the following steps using Ref. [18].

1. The in-plane fluid flow equation is given as

$$u_x = \frac{1}{2\mu}\frac{\partial p}{\partial x}\left(y^2 - hy\right) + U_1\left(1 - \frac{y}{h}\right) + U_2\left(\frac{y}{h}\right) \tag{44}$$

$$u_z = \frac{1}{2\mu}\frac{\partial p}{\partial z}\left(y^2 - hy\right), \tag{45}$$

where U_1, U_2 respectively represent the local rotor speed and bearing speed.

2. Integrate continuity equation along the y coordinate

$$\int_0^y \left(\frac{\partial \rho}{\partial t} + \frac{\partial \rho u_x}{\partial x} + \frac{\partial \rho u_y}{\partial y} + \frac{\partial \rho u_z}{\partial z}\right) \mathrm{d}y = 0. \tag{46}$$

In the case of no nozzle entry,

$$[\rho u_y]_0^y = \rho \frac{dh}{dt} \tag{47}$$

3. Replacing u_x and u_z by Eqs. (44) and (45) in Eq. (46), the following equations is obtained:

$$\frac{\partial}{\partial x}\left(\frac{\rho h^3}{12\mu}\frac{\partial p}{\partial x}\right) + \frac{\partial}{\partial z}\left(\frac{\rho h^3}{12\mu}\frac{\partial p}{\partial z}\right) = \frac{1}{2}\frac{\partial\left(\rho h U_0\right)}{\partial x} + \frac{\partial(\rho h)}{\partial t}, \tag{48}$$

where $U_0 = (U_1 + U_2)$.

4. In case of fluid flow through a nozzle entry, the integrated Eq. (46) becomes

$$\frac{\partial}{\partial x}\left(\frac{\rho h^3}{12\mu}\frac{\partial p}{\partial x}\right) + \frac{\partial}{\partial z}\left(\frac{\rho h^3}{12\mu}\frac{\partial p}{\partial z}\right) = \frac{1}{2}\frac{\partial\left(\rho h U_0\right)}{\partial x} + \frac{\partial(\rho h)}{\partial t} - S^{nozzle}, \tag{49}$$

where the source term S^{nozzle} is such that

$$\dot{m} = \int_{A_n} S^{nozzle} \mathrm{d}A_n. \tag{50}$$

Here A_n denotes the nozzle area opening.

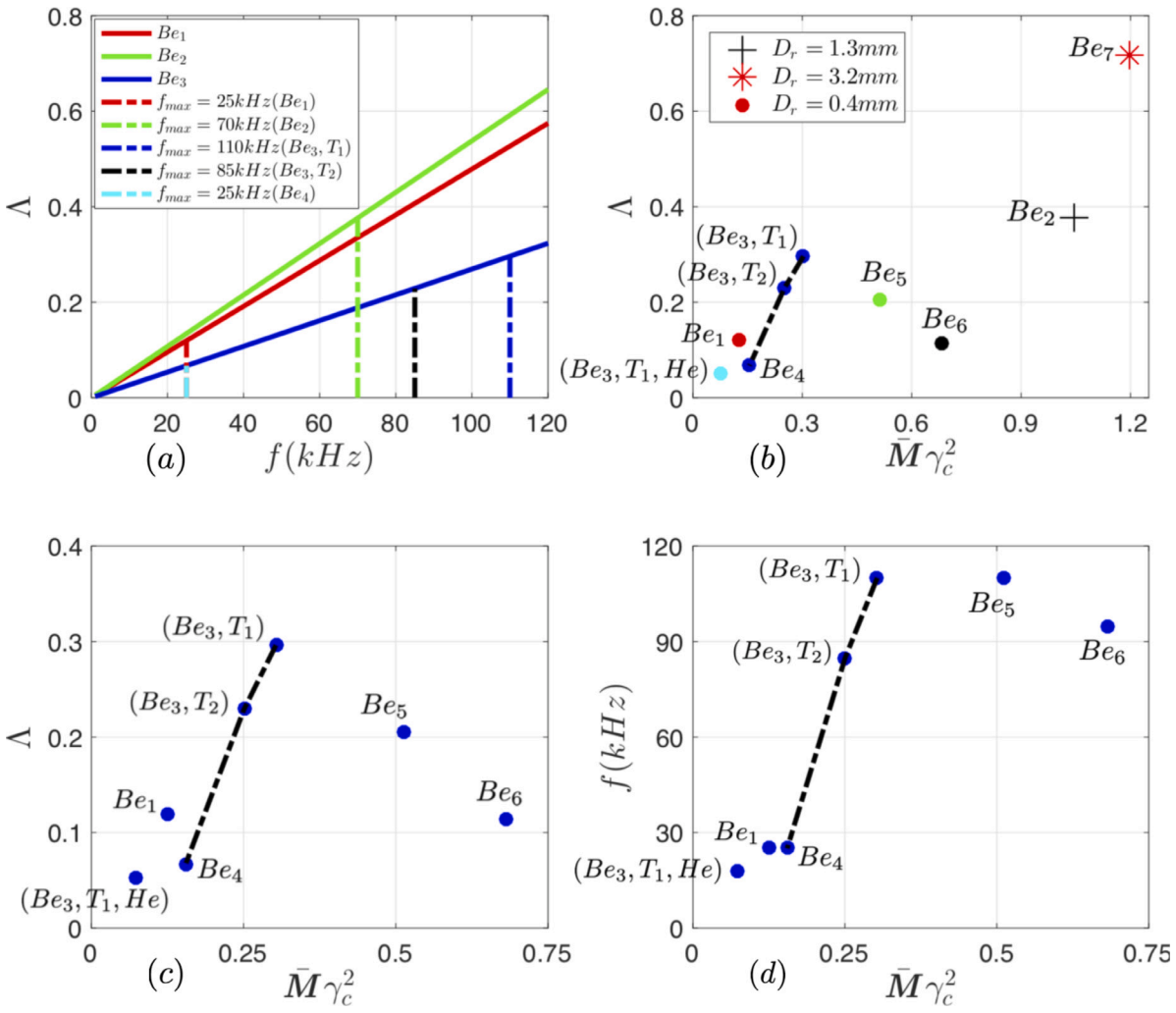

Fig. 20. Figure (*a*) depicts Λ vs. f for bearing types Be_1, Be_2 and Be_3. The dashed lines mark the bearing number corresponding to maximum stable frequency (obtained experimentally). Figure (*b*) shows experimentally obtained values of maximum stable bearing numbers against the numerical solutions of critical inertial force for different bearing types. Figure (*c*) compares the experimentally obtained values of maximum stable bearing numbers against the numerical solutions of critical inertial force for one family of bearings applied to rotor size $D_r = 0.4$ mm. Figure (*d*) plots the maximum stable frequency against the maximum stable inertial force for the family of bearings applied to rotor size $D_r = 0.4$ mm. (For interpretation of the references to color in this figure legend, the reader is referred to the web version of this article.)

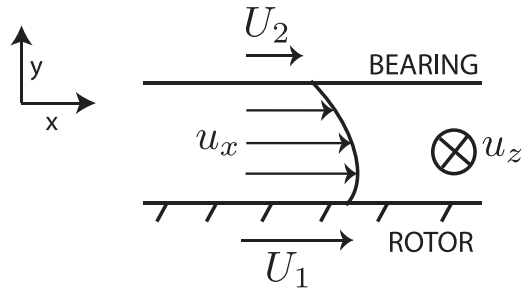

Fig. 21. The local coordinate (x, y, z) for the flow in the bearing–rotor gap.

5. For cylindrical coordinate, the dimensional Reynolds equation (49) becomes

$$\frac{1}{R^2}\frac{\partial}{\partial\theta}\left(\frac{\rho h^3}{12\mu}\frac{\partial p}{\partial\theta}\right)+\frac{\partial}{\partial z}\left(\frac{\rho h^3}{12\mu}\frac{\partial p}{\partial z}\right)=\frac{1}{2}\frac{\partial(\rho h U_0)}{R\partial\theta}+\frac{\partial(\rho h)}{\partial t}-S^{nozzle} \quad (51)$$

$$\text{where } U_0 = \omega_r R. \quad (52)$$

For the rest of the derivation, it is assumed that $R \approx R_b$, where R_b is the bearing radius.

6. For the gas, using isothermal condition leads to

$$\frac{p}{\rho} = R^0 T^0. \quad (53)$$

Setting relation (53) to Eq. (51) leads to

$$\frac{1}{R_b^2}\frac{\partial}{\partial\theta}\left(\frac{h^3}{24\mu}\frac{\partial p^2}{\partial\theta}\right)+\frac{\partial}{\partial z}\left(\frac{h^3}{24\mu}\frac{\partial p^2}{\partial z}\right) = \frac{1}{2}\frac{\partial(ph\omega_r R_b)}{R_b\partial\theta}+\frac{\partial(ph)}{\partial t}-R^0T^0S^{nozzle}. \quad (54)$$

7. Finally non-dimensionalization using $h = c\bar{h}$, $P = p_a\bar{P}$, $z = L\bar{z}$ and $t = \gamma\omega_r\tau$ in (54) leads to

$$\frac{\partial}{\partial\theta}\left[\bar{h}^3\frac{\partial\bar{P}^2}{\partial\theta}\right]+\frac{1}{4\lambda^2}\frac{\partial}{\partial\bar{z}}\left[\bar{h}^3\frac{\partial\bar{P}^2}{\partial\bar{z}}\right] = 2\Lambda\frac{\partial}{\partial\theta}\left(\bar{P}\bar{h}\right)+4\gamma\Lambda\frac{\partial}{\partial\tau}\left(\bar{P}\bar{h}\right)-\left(\frac{24\mu R^0T^0R_b^2}{P_a^2c^3}\right)S^{nozzle}, \quad (55)$$

where the terms Λ and λ are defined by Eqs. (5) and (7) respectively.

8. Integrating the source term over a dimensionless area $\bar{A}_n = A_n/(R_b L)$ leads to

$$\left(\frac{24\mu R^0 T^0 R_b^2}{P_a^2 c^3}\right)\int_{\bar{A}_n} S^{nozzle}\mathrm{d}\theta\mathrm{d}\bar{z} = \left(\frac{24\mu R^0 T^0 R_b}{P_a^2 c^3 L}\right)\int_{A_n} S^{nozzle}\mathrm{d}A_n, \tag{56}$$

$$\text{where } \mathrm{d}A_n = R_b\mathrm{d}\theta\mathrm{d}z = R_b L\mathrm{d}\theta\mathrm{d}\bar{z} \tag{57}$$

9. Setting Eqs. (50) and (11) to Eq. (56) leads to

$$\left(\frac{24\mu R^0 T^0 R_b^2}{P_a^2 c^3}\right)\int_{\bar{A}_n} S^{nozzle}\mathrm{d}\theta\mathrm{d}\bar{z} = \left(\frac{24\mu R^0 T^0 R_b}{P_a^2 c^3 L}\right)\frac{C_d A_n p_s \delta}{\sqrt{R^0 T^0}} = \left(\frac{R_b}{L}\right)\left(\frac{24\mu C_d A_n\sqrt{R^0 T^0}}{P_a c^3}\right)\left(\frac{p_s}{P_a}\right)\delta \tag{58}$$

10. Using the definition of λ, Γ_0 and $\bar{Q}_r$ from Eqs. (7), (15) and (14) respectively, replacing nozzle area A_n by $\pi d_n^2/4$ and using $\bar{P}_s = (p_s/p_a)$ in Eq. (58), the following relation is obtained:

$$\left(\frac{24\mu R^0 T^0 R_b^2}{P_a^2 c^3}\right)\int_{\bar{A}_n} S^{nozzle}\mathrm{d}\bar{A}_n = \frac{1}{8\lambda}\Gamma_0\bar{P}_s\delta = \frac{1}{8\lambda}\int_{\bar{A}_n}\bar{Q}_r\mathrm{d}\bar{A}_n \tag{59}$$

The derivation of Reynolds equation with nozzle entry can be modified for relatively large nozzle size by assuming large nozzle to be a combination of infinitely large number of small streamlines. For each of such streamlines, the local averaged fluid pressure in the viscous sublayer is used as the nozzle exit pressure. The assumption leads to

$$\dot{m} = \int_{A_n}\frac{C_d p_s\delta}{\sqrt{R^0 T^0}}\mathrm{d}A_n \text{ and therefore} \tag{60}$$

$$S^{nozzle} = \frac{\mathrm{d}\dot{m}}{\mathrm{d}A_n} = \frac{C_d p_s\delta}{\sqrt{R^0 T^0}}. \tag{61}$$

For finite sized nozzle, setting definition (61) to Eq. (55) leads to

$$\frac{\partial}{\partial\theta}\left[\bar{h}^3\frac{\partial\bar{P}^2}{\partial\theta}\right] + \frac{1}{4\lambda^2}\frac{\partial}{\partial\bar{z}}\left[\bar{h}^3\frac{\partial\bar{P}^2}{\partial\bar{z}}\right] = 2\Lambda\frac{\partial}{\partial\theta}\left(\bar{P}\bar{h}\right) + 4\gamma\Lambda\frac{\partial}{\partial\tau}\left(\bar{P}\bar{h}\right) - \left(\frac{24\mu R^0 T^0 R_b^2}{P_a^2 c^3}\right)\frac{C_d p_s\delta}{\sqrt{R^0 T^0}}, \tag{62}$$

which after rearrangement yields

$$\frac{\partial}{\partial\theta}\left[\bar{h}^3\frac{\partial\bar{P}^2}{\partial\theta}\right] + \frac{1}{4\lambda^2}\frac{\partial}{\partial\bar{z}}\left[\bar{h}^3\frac{\partial\bar{P}^2}{\partial\bar{z}}\right] = 2\Lambda\frac{\partial}{\partial\theta}\left(\bar{P}\bar{h}\right) + 4\gamma\Lambda\frac{\partial}{\partial\tau}\left(\bar{P}\bar{h}\right) - \left(\frac{R_b^2}{\pi d_n^2}\right)\left(\frac{24\mu C_d\pi d_n^2\sqrt{R^0 T^0}}{P_a c^3}\right)\left(\frac{p_s}{P_a}\right)\delta. \tag{63}$$

Finally using the definition of Γ_0 and $\bar{Q}_r^{finite}$ from Eqs. (15) and (18) respectively in Eq. (63) leads to the non-dimensionalized Reynolds equation for finite sized nozzle

$$\frac{\partial}{\partial\theta}\left[\bar{h}^3\frac{\partial\bar{P}^2}{\partial\theta}\right] + \frac{1}{4\lambda^2}\frac{\partial}{\partial\bar{z}}\left[\bar{h}^3\frac{\partial\bar{P}^2}{\partial\bar{z}}\right] = 2\Lambda\frac{\partial}{\partial\theta}\left(\bar{P}\bar{h}\right) + 4\gamma\Lambda\frac{\partial}{\partial\tau}\left(\bar{P}\bar{h}\right) - \left(\frac{R_b^2}{\pi d_n^2}\right)\bar{Q}_r^{finite}. \tag{64}$$

Appendix B

The governing Reynolds equation of linearly perturbed pressure is derived in this section. This derivation follows closely the perturbed system for whirl instability derived by Lund [12]. In the following perturbed pressure and the corresponding stiffness and damping calculations are given.

1. A new variable denoted as S and is defined by

$$S = \left(\bar{P}\bar{h}\right)^2, \tag{65}$$

where using the terms

$$\frac{\partial S}{\partial\theta} = \bar{h}^2\frac{\partial\bar{P}^2}{\partial\theta} + 2\bar{P}^2\bar{h}\frac{\partial\bar{h}}{\partial\theta} \tag{66}$$

$$\text{and } \frac{\partial S}{\partial\bar{z}} = \bar{h}^2\frac{\partial\bar{P}^2}{\partial\bar{z}} + 2\bar{P}^2\bar{h}\frac{\partial\bar{h}}{\partial\bar{z}} \tag{67}$$

in

$$\bar{h}^3\frac{\partial\bar{P}^2}{\partial\theta} = \bar{h}\frac{\partial S}{\partial\theta} - 2S\frac{\partial\bar{h}}{\partial\theta} \tag{68}$$

$$\text{and } \bar{h}^3\frac{\partial\bar{P}^2}{\partial\bar{z}} = \bar{h}\frac{\partial S}{\partial\bar{z}} - 2S\frac{\partial\bar{h}}{\partial\bar{z}} \text{ respectively,} \tag{69}$$

the left hand side of Reynolds equation (17) can be reformulated as

$$\frac{\partial}{\partial\theta}\left[\bar{h}^3\frac{\partial\bar{P}^2}{\partial\theta}\right] + \frac{1}{4\lambda^2}\frac{\partial}{\partial\bar{z}}\left[\bar{h}^3\frac{\partial\bar{P}^2}{\partial\bar{z}}\right] = \bar{h}\tilde{\nabla}^2 S - 2S\tilde{\nabla}^2\bar{h} - \left(\frac{\partial S}{\partial\theta}\frac{\partial\bar{h}}{\partial\theta} + \frac{1}{4\lambda^2}\frac{\partial S}{\partial\bar{z}}\frac{\partial\bar{h}}{\partial\bar{z}}\right) \tag{70}$$

$$\text{where } \tilde{\nabla}^2 = \left[\frac{\partial^2}{\partial\theta^2} + \frac{1}{4\lambda^2}\frac{\partial^2}{\partial\bar{z}^2}\right]. \tag{71}$$

Using relation (70) in Reynolds Eq. (17) leads to

$$\bar{h}\tilde{\nabla}^2 S - 2S\tilde{\nabla}^2\bar{h} - \left(\frac{\partial S}{\partial\theta}\frac{\partial\bar{h}}{\partial\theta} + \frac{1}{4\lambda^2}\frac{\partial S}{\partial\bar{z}}\frac{\partial\bar{h}}{\partial\bar{z}}\right) = 2\Lambda\frac{\partial}{\partial\theta}\left(\bar{P}\bar{h}\right) + 4\gamma\Lambda\frac{\partial}{\partial\tau}\left(\bar{P}\bar{h}\right) - \left(\frac{R_b^2}{\pi d_n^2}\right)\bar{Q}_r. \tag{72}$$

2. A perturbation of equilibrium eccentricity (ε_0) and attitude angle (ϕ_0) leads to the change in the equilibrium normalized gap solution,

$$\bar{h}_0 = 1 + \varepsilon_0\cos(\theta - \phi_0) \tag{73}$$

to the following value of perturbed gap thickness:

$$\bar{h} = 1 + (\varepsilon_0 + \boldsymbol{\varepsilon_p})\cos(\theta - \phi_0 - \boldsymbol{\phi_p}), \tag{74}$$

where $\boldsymbol{\varepsilon_p}$ and $\boldsymbol{\phi_p}$ are perturbed values of equilibrium eccentricity and attitude angle respectively. The assumption of small perturbation leads to

$$\cos\boldsymbol{\phi_p} \approx 1 \tag{75}$$

$$\sin\boldsymbol{\phi_p} \approx \boldsymbol{\phi_p} \tag{76}$$

$$\boldsymbol{\varepsilon_p}\boldsymbol{\phi_p} \approx 0, \tag{77}$$

which reduces the perturbed Eq. (74) to

$$\bar{h} = 1 + \varepsilon_0\cos\bar{\theta} + \varepsilon_0\boldsymbol{\phi_p}\sin\bar{\theta} + \boldsymbol{\varepsilon_p}\cos\bar{\theta} \tag{78}$$

$$\text{where } \bar{\theta} = (\theta - \phi_0). \tag{79}$$

Using definition of $\bar{h}_0$ and $\bar{\theta}$ from Eqs. (73) and (79) in Eq. (78) leads to

$$\bar{h} = \bar{h}_0 + \boldsymbol{\varepsilon_p}\cos\bar{\theta} + \varepsilon_0\boldsymbol{\phi_p}\sin\bar{\theta}. \tag{80}$$

Assuming fluctuating nature of perturbed parameters, the following solution for perturbed parameters can be taken into account:

$$\boldsymbol{\varepsilon_p} = \varepsilon_p\exp(\hat{\jmath}\tau) \tag{81}$$

$$\boldsymbol{\phi_p} = \phi_p\exp(\hat{\jmath}\tau), \tag{82}$$

which leads to the perturbed gap thickness solution (19). The term τ in Eqs. (81) and (82) denotes the dimensionless time ($\tau = \Omega t$). Using this perturbed solution for gap thickness and the ansatz for perturbed pressure solution (20), the perturbed part of S can be approximated as

$$S_p \approx \left(\bar{P}_0\bar{h}_0\right)^2 + 2\bar{P}_0\bar{h}_0\left(\varepsilon_p\exp(\hat{\jmath}\tau)\cos\bar{\theta} + \varepsilon_0\phi_p\exp(\hat{\jmath}\tau)\sin\bar{\theta}\right) + \tag{83}$$

$$2\bar{P}_0\bar{h}_0\left(\varepsilon_p \exp(\hat{j}\tau)\bar{P}_\varepsilon + \varepsilon_0\phi_p \exp(\hat{j}\tau)\bar{P}_\phi\right),$$

where the terms containing $\left(\varepsilon_p^a\phi_p^b\right)$ with $(a+b)>1$ are neglected and $S \approx (S_0 + S_p)$.

3. The perturbed solution (83) can be re-expressed as

$$\begin{aligned} S_p = &\left(\bar{P}_0\bar{h}_0\right)^2 + 2\varepsilon_p \exp(\hat{j}\tau)\bar{P}_0\bar{h}_0\left(\bar{P}_0\cos\bar{\theta} + \bar{P}_\varepsilon\bar{h}_0\right) \\ &+ 2\varepsilon_0\phi_p \exp(\hat{j}\tau)\bar{P}_0\bar{h}_0\left(\bar{P}_0\sin\bar{\theta} + \bar{P}_\phi\bar{h}_0\right). \end{aligned} \tag{84}$$

Using the following definitions

$$S_0 = \left(\bar{P}_0\bar{h}_0\right)^2, \tag{85}$$

$$S_\varepsilon = \bar{P}_0\bar{h}_0\left(\bar{P}_0\cos\bar{\theta} + \bar{P}_\varepsilon\bar{h}_0\right) \tag{86}$$

$$\text{and } S_\phi = \bar{P}_0\bar{h}_0\left(\bar{P}_0\sin\bar{\theta} + \bar{P}_\phi\bar{h}_0\right), \tag{87}$$

the perturbed Eq. (84) can be written as

$$S_p = S_0 + 2\varepsilon_p \exp(\hat{j}\tau)S_\varepsilon + 2\varepsilon_0\phi_p \exp(\hat{j}\tau)S_\phi. \tag{88}$$

4. Using Eqs. (19) and (20), the term $\bar{P}\bar{h}$ can be approximated as

$$\begin{aligned} \bar{P}\bar{h} \approx\ & \bar{P}_0\bar{h}_0 + \varepsilon_p \exp(\hat{j}\tau)\left(\bar{P}_0\cos\bar{\theta} + \bar{P}_\varepsilon\bar{h}_0\right) + \varepsilon_0\phi_p \exp(\hat{j}\tau) \\ &\times \left(\bar{P}_0\sin\bar{\theta} + \bar{P}_\phi\bar{h}_0\right), \end{aligned} \tag{89}$$

where the terms containing $\left(\varepsilon_p^a\phi_p^b\right)$ with $(a+b) > 1$ are neglected. Using relations

$$\left(\bar{P}_0\cos\bar{\theta} + \bar{P}_\varepsilon\bar{h}_0\right) = S_\varepsilon/\sqrt{S_0} \tag{90}$$

$$\text{and } \left(\bar{P}_0\sin\bar{\theta} + \bar{P}_\phi\bar{h}_0\right) = S_\phi/\sqrt{S_0} \tag{91}$$

in Eq. (89), the following relation is obtained.

$$\bar{P}\bar{h} = \sqrt{S_0} + \varepsilon_p \exp(\hat{j}\tau)\left(S_\varepsilon/\sqrt{S_0}\right) + \varepsilon_0\phi_p \exp(\hat{j}\tau)\left(S_\phi/\sqrt{S_0}\right) \tag{92}$$

5. The nozzle mass flow model is given as

$$\bar{Q}_r = \Gamma_0\bar{P}_s\delta(\bar{P}). \tag{93}$$

The Taylor expansion of $\delta(\bar{P})$ about the equilibrium point $\bar{P}_0$ in Eq. (93) leads to

$$\begin{aligned} \bar{Q}_r = &\Gamma_0\bar{P}_s\left(\delta(\bar{P}_0) + \left(\frac{\partial\delta}{\partial P}\right)_0\left(\bar{P}-\bar{P}_0\right) + \frac{1}{2!}\left(\frac{\partial^2\delta}{\partial P^2}\right)_0\left(\bar{P}-\bar{P}_0\right)^2\right. \\ &\left. + \frac{1}{3!}\left(\frac{\partial^3\delta}{\partial P^3}\right)_0\left(\bar{P}-\bar{P}_0\right)^3 + \cdots\right). \end{aligned} \tag{94}$$

Neglecting terms containing $\left(\bar{P}-\bar{P}_0\right)^a$ with $a > 1$ in Eq. (94) leads to

$$\bar{Q}_r = \Gamma_0\bar{P}_s\left(\delta_0 + \left(\frac{\partial\delta}{\partial P}\right)_0\left(\bar{P}-\bar{P}_0\right)\right). \tag{95}$$

Setting perturbed pressure ansatz (20) to Eq. (95) yields

$$\bar{Q}_r = \Gamma_0\bar{P}_s\delta_0 + \varepsilon_p \exp(\hat{j}\tau)\left(\frac{\partial\delta}{\partial P}\right)_0\Gamma_0\bar{P}_s\bar{P}_\varepsilon + \varepsilon_0\phi_p \exp(\hat{j}\tau)\left(\frac{\partial\delta}{\partial P}\right)_0\Gamma_0\bar{P}_s\bar{P}_\phi. \tag{96}$$

The Eq. (96) can be re-expressed as

$$\bar{Q}_r = \bar{Q}_{r0} + \varepsilon_p \exp(\hat{j}\tau)\bar{Q}_{r\varepsilon} + \varepsilon_0\phi_p \exp(\hat{j}\tau)\bar{Q}_{r\phi} \tag{97}$$

$$\text{where } \bar{Q}_{r0} = \Gamma_0\bar{P}_s\delta_0, \tag{98}$$

$$\bar{Q}_{r\varepsilon} = \left(\frac{\partial\delta}{\partial P}\right)_0\Gamma_0\bar{P}_s\bar{P}_\varepsilon \tag{99}$$

$$\text{and } \bar{Q}_{r\phi} = \left(\frac{\partial\delta}{\partial P}\right)_0\Gamma_0\bar{P}_s\bar{P}_\phi. \tag{100}$$

The term $\bar{h}_0$ is independent of $\bar{z}$ and the terms S_ε, S_ϕ and S_0 are independent of τ. These, therefore lead to

$$\frac{\partial\bar{h}_0}{\partial\bar{z}} = \frac{\partial S_\varepsilon}{\partial\tau} = \frac{\partial S_\phi}{\partial\tau} = \frac{\partial S_0}{\partial\tau} = 0. \tag{101}$$

6. Using Eqs. (88), (92), (97) and (101) in Eq. (72), the following equations for perturbed components of S are obtained.

$$\begin{aligned} &\bar{\nabla}^2 S_\varepsilon - \frac{1}{\bar{h}_0}\left(\frac{\partial\bar{h}_0}{\partial\theta} + \frac{\Lambda}{\sqrt{S_0}}\right)\frac{\partial S_\varepsilon}{\partial\theta} \\ &-\frac{1}{\bar{h}_0}\left(2\frac{\partial^2\bar{h}_0}{\partial\theta^2} - \frac{\Lambda}{2S_0^{3/2}}\frac{\partial S_0}{\partial\theta} + \frac{2\hat{j}\gamma\Lambda}{\sqrt{S_0}}\right) \\ &\times S_\varepsilon = -\left(\frac{\cos\bar{\theta}}{2\bar{h}_0}\right)\bar{\nabla}^2 S_0 \\ &-\left(\frac{\sin\bar{\theta}}{2\bar{h}_0}\right)\frac{\partial S_0}{\partial\theta} - \left(\frac{\cos\bar{\theta}}{\bar{h}_0}\right)S_0 - \left(\frac{R_b^2}{2\pi\bar{h}_0 d_n^2}\right)\bar{Q}_{r\varepsilon} \end{aligned} \tag{102}$$

$$\begin{aligned} &\bar{\nabla}^2 S_\phi - \frac{1}{\bar{h}_0}\left(\frac{\partial\bar{h}_0}{\partial\theta} + \frac{\Lambda}{\sqrt{S_0}}\right)\frac{\partial S_\phi}{\partial\theta} - \frac{1}{\bar{h}_0} \\ &\times\left(2\frac{\partial^2\bar{h}_0}{\partial\theta^2} - \frac{\Lambda}{2S_0^{3/2}}\frac{\partial S_0}{\partial\theta} + \frac{2\hat{j}\gamma\Lambda}{\sqrt{S_0}}\right) \\ &\times S_\phi = -\left(\frac{\sin\bar{\theta}}{2\bar{h}_0}\right)\bar{\nabla}^2 S_0 \\ &+\left(\frac{\cos\bar{\theta}}{2\bar{h}_0}\right)\frac{\partial S_0}{\partial\theta} - \left(\frac{\sin\bar{\theta}}{\bar{h}_0}\right)S_0 - \left(\frac{R_b^2}{2\pi\bar{h}_0 d_n^2}\right)\bar{Q}_{r\phi} \end{aligned} \tag{103}$$

7. Using Eq. (12) in Eqs. (99) and (100), the terms $\bar{Q}_{r\varepsilon}$ and $\bar{Q}_{r\phi}$ can be expressed as

$$\bar{Q}_{r\varepsilon} = \begin{cases} \frac{\Gamma_0\bar{P}_\varepsilon}{\sqrt{2\kappa(\kappa-1)}}\frac{\left[2\left(\frac{p_r}{p_s}\right)^{(2-\kappa)/\kappa} - (\kappa+1)\left(\frac{p_r}{p_s}\right)^{1/\kappa}\right]}{\sqrt{\left[\left(\frac{p_r}{p_s}\right)^{2/\kappa} - \left(\frac{p_r}{p_s}\right)^{(\kappa+1)/\kappa}\right]}}, \text{ for subsonic conditions and} \\ 0, \text{ for supersonic conditions.} \end{cases} \tag{104}$$

and

$$\bar{Q}_{r\phi} = \begin{cases} \frac{\Gamma_0\bar{P}_\phi}{\sqrt{2\kappa(\kappa-1)}}\frac{\left[2\left(\frac{p_r}{p_s}\right)^{(2-\kappa)/\kappa} - (\kappa+1)\left(\frac{p_r}{p_s}\right)^{1/\kappa}\right]}{\sqrt{\left[\left(\frac{p_r}{p_s}\right)^{2/\kappa} - \left(\frac{p_r}{p_s}\right)^{(\kappa+1)/\kappa}\right]}}, \text{ for subsonic conditions and} \\ 0, \text{ for supersonic conditions.} \end{cases} \tag{105}$$

The perturbed force components F_x^p and F_y^p applied on the rotor along x and y directions due to fluid pressure as illustrated in the part (a) of Fig. 22 are given as

$$F_x^p = -\int_0^{2\pi}\int_0^L p_a\left(\boldsymbol{\varepsilon_p}\bar{P}_\varepsilon + \varepsilon_0\boldsymbol{\phi_p}\bar{P}_\phi\right)\sin\theta\left(R_b\mathrm{d}\theta\mathrm{d}z\right) \tag{106}$$

$$\text{and } F_y^p = -\int_0^{2\pi}\int_0^L p_a\left(\boldsymbol{\varepsilon_p}\bar{P}_\varepsilon + \varepsilon_0\boldsymbol{\phi_p}\bar{P}_\phi\right)\cos\theta\left(R_b\mathrm{d}\theta\mathrm{d}z\right). \tag{107}$$

Non-dimensionalization of the perturbed force components using the term $(2R_bLp_a)$ yields the dimensionless perturbed force components

$$\begin{aligned} \bar{F}_x^p = &-\frac{1}{2}\boldsymbol{\varepsilon_p}\int_0^{2\pi}\int_0^1\bar{P}_\varepsilon\sin\theta d\theta d\bar{z} - \frac{1}{2}\varepsilon_0\boldsymbol{\phi_p} \\ &\times\int_0^{2\pi}\int_0^1\bar{P}_\phi\sin\theta d\theta d\bar{z} \end{aligned} \tag{108}$$

$$\begin{aligned} \text{and } \bar{F}_y^p = &-\frac{1}{2}\boldsymbol{\varepsilon_p}\int_0^{2\pi}\int_0^1\bar{P}_\varepsilon\cos\theta d\theta d\bar{z} - \frac{1}{2}\varepsilon_0\boldsymbol{\phi_p} \\ &\times\int_0^{2\pi}\int_0^1\bar{P}_\phi\cos\theta d\theta d\bar{z} \end{aligned} \tag{109}$$

along the $\bar{x}$ and $\bar{y}$ directions respectively. The terms $\boldsymbol{\varepsilon_p}$ and $\varepsilon_0\boldsymbol{\phi_p}$ are obtained via coordinate transformation of $(\bar{x},\bar{y})$ axes by counterclockwise rotation angle of $(\pi-\phi_0)$ as presented in the part (b) of Fig. 22. Therefore,

$$\begin{bmatrix}\varepsilon_0\boldsymbol{\phi_p}\\ \boldsymbol{\varepsilon_p}\end{bmatrix} = \begin{bmatrix}\cos(\pi-\phi_0) & \sin(\pi-\phi_0)\\ -\sin(\pi-\phi_0) & \cos(\pi-\phi_0)\end{bmatrix}\begin{bmatrix}\bar{x}\\ \bar{y}\end{bmatrix}, \text{ which yields} \tag{110}$$

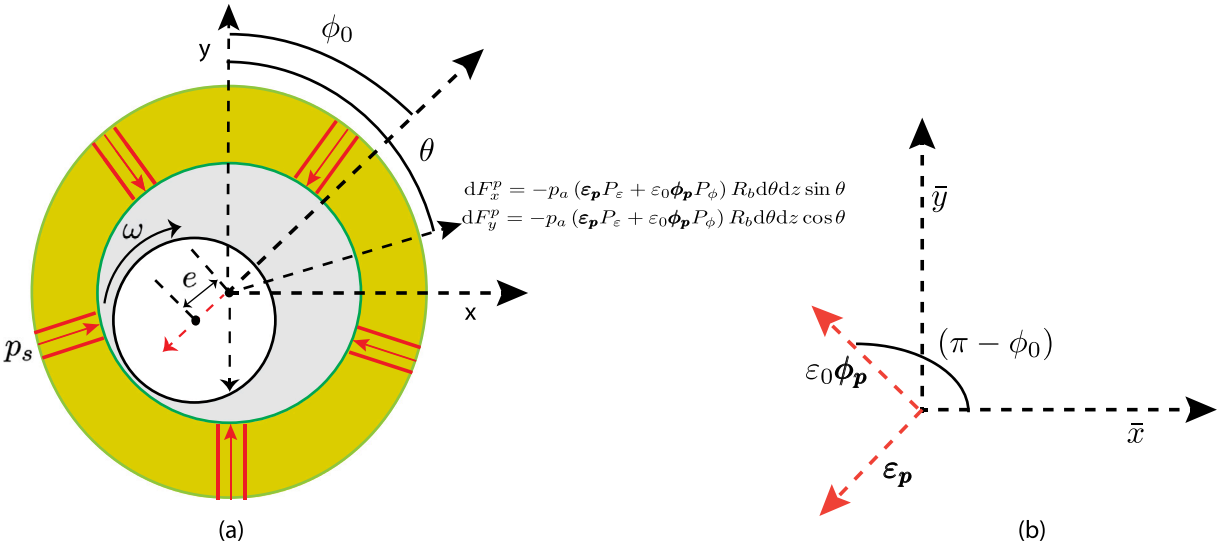

Fig. 22. The left figure shows the direction of applied force on a differential area segment ($R_b \mathrm{d}\theta \mathrm{d}z$) of the rotor. The right figure shows the coordinate transformation from $(\bar{x}, \bar{y})$ axes to $(\varepsilon_0 \boldsymbol{\phi}_p, \boldsymbol{\varepsilon}_p)$ axes.

$$\boldsymbol{\varepsilon}_p = \left(-\bar{x}\sin\phi_0 - \bar{y}\cos\phi_0\right) \tag{111}$$

$$\text{and } \varepsilon_0 \boldsymbol{\phi}_p = \left(-\bar{x}\cos\phi_0 + \bar{y}\sin\phi_0\right). \tag{112}$$

Setting the definitions (111) and (112) to Eqs. (108) and (109) and using $\theta = (\bar{\theta} + \phi_0)$, the non-dimensionalized force equations can be reformulated as

$$\begin{aligned}\bar{F}_x^p &= \frac{1}{2}\left(\bar{x}\sin\phi_0 + \bar{y}\cos\phi_0\right)\int_{-\phi_0}^{2\pi-\phi_0}\int_0^1 \bar{P}_\varepsilon \sin\left(\bar{\theta}+\phi_0\right)\mathrm{d}\bar{\theta}\mathrm{d}\bar{z} \\ &+\frac{1}{2}\left(\bar{x}\cos\phi_0 - \bar{y}\sin\phi_0\right)\int_{-\phi_0}^{2\pi-\phi_0}\int_0^1 \bar{P}_\phi \sin\left(\bar{\theta}+\phi_0\right)\mathrm{d}\bar{\theta}\mathrm{d}\bar{z} \end{aligned} \tag{113}$$

$$\begin{aligned}\text{and } \bar{F}_y^p &= \frac{1}{2}\left(\bar{x}\sin\phi_0 + \bar{y}\cos\phi_0\right)\int_{-\phi_0}^{2\pi-\phi_0}\int_0^1 \bar{P}_\varepsilon \cos\left(\bar{\theta}+\phi_0\right)\mathrm{d}\bar{\theta}\mathrm{d}\bar{z} \\ &+\frac{1}{2}\left(\bar{x}\cos\phi_0 - \bar{y}\sin\phi_0\right)\int_{-\phi_0}^{2\pi-\phi_0}\int_0^1 \bar{P}_\phi \cos\left(\bar{\theta}+\phi_0\right) \\ &\times \mathrm{d}\bar{\theta}\mathrm{d}\bar{z}. \end{aligned} \tag{114}$$

Using the periodicity of pressure perturbation components $\bar{P}_\varepsilon$ and $\bar{P}_\phi$, the Eqs. (113) and (114) can be rearranged as

$$\begin{aligned}\bar{F}_x^p &= \bar{x}\left[\left(\frac{1}{2}\sin\phi_0\sin\phi_0\int_0^{2\pi}\int_0^1 \bar{P}_\varepsilon\cos\bar{\theta}\right)\right. \\ &\left.+\left(\frac{1}{2}\sin\phi_0\cos\phi_0\int_0^{2\pi}\int_0^1 \bar{P}_\varepsilon\sin\bar{\theta}\right)\right]+ \\ &\bar{x}\left[\left(\frac{1}{2}\sin\phi_0\cos\phi_0\int_0^{2\pi}\int_0^1 \bar{P}_\phi\cos\bar{\theta}\right)\right. \\ &\left.+\left(\frac{1}{2}\cos\phi_0\cos\phi_0\int_0^{2\pi}\int_0^1 \bar{P}_\phi\sin\bar{\theta}\right)\right]+ \\ &\bar{y}\left[\left(\frac{1}{2}\cos\phi_0\sin\phi_0\int_0^{2\pi}\int_0^1 \bar{P}_\varepsilon\cos\bar{\theta}\right)\right. \\ &\left.+\left(\frac{1}{2}\cos\phi_0\cos\phi_0\int_0^{2\pi}\int_0^1 \bar{P}_\varepsilon\sin\bar{\theta}\right)\right]- \\ &\bar{y}\left[\left(\frac{1}{2}\sin\phi_0\sin\phi_0\int_0^{2\pi}\int_0^1 \bar{P}_\phi\cos\bar{\theta}\right)\right. \\ &\left.+\left(\frac{1}{2}\sin\phi_0\cos\phi_0\int_0^{2\pi}\int_0^1 \bar{P}_\phi\sin\bar{\theta}\right)\right] \end{aligned} \tag{115}$$

$$\begin{aligned}\text{and } \bar{F}_y^p &= \bar{x}\left[\left(\frac{1}{2}\sin\phi_0\cos\phi_0\int_0^{2\pi}\int_0^1 \bar{P}_\varepsilon\cos\bar{\theta}\right)\right. \\ &\left.-\left(\frac{1}{2}\sin\phi_0\sin\phi_0\int_0^{2\pi}\int_0^1 \bar{P}_\varepsilon\sin\bar{\theta}\right)\right]+ \\ &\bar{x}\left[\left(\frac{1}{2}\cos\phi_0\cos\phi_0\int_0^{2\pi}\int_0^1 \bar{P}_\phi\cos\bar{\theta}\right)\right. \\ &\left.-\left(\frac{1}{2}\sin\phi_0\cos\phi_0\int_0^{2\pi}\int_0^1 \bar{P}_\phi\sin\bar{\theta}\right)\right]+ \\ &\bar{y}\left[\left(\frac{1}{2}\cos\phi_0\cos\phi_0\int_0^{2\pi}\int_0^1 \bar{P}_\varepsilon\cos\bar{\theta}\right)\right. \\ &\left.-\left(\frac{1}{2}\sin\phi_0\cos\phi_0\int_0^{2\pi}\int_0^1 \bar{P}_\varepsilon\sin\bar{\theta}\right)\right]- \\ &\bar{y}\left[\left(\frac{1}{2}\sin\phi_0\cos\phi_0\int_0^{2\pi}\int_0^1 \bar{P}_\phi\cos\bar{\theta}\right)\right. \\ &\left.-\left(\frac{1}{2}\sin\phi_0\sin\phi_0\int_0^{2\pi}\int_0^1 \bar{P}_\phi\sin\bar{\theta}\right)\right]. \end{aligned} \tag{116}$$

Using the definition of stiffness given in Eq. (3), the following relations for the stiffness components are obtained from Eqs. (115) and (116).

$$\begin{aligned}K_{xx} &= (\sin\phi_0\sin\phi_0)\bar{K}_{\varepsilon\varepsilon} + (\sin\phi_0\cos\phi_0)\bar{K}_{\varepsilon\phi} \\ &+(\sin\phi_0\cos\phi_0)\bar{K}_{\phi\varepsilon} + (\cos\phi_0\cos\phi_0)\bar{K}_{\phi\phi} \end{aligned} \tag{117}$$

$$\begin{aligned}K_{yx} &= (\cos\phi_0\sin\phi_0)\bar{K}_{\varepsilon\varepsilon} + (\cos\phi_0\cos\phi_0)\bar{K}_{\varepsilon\phi} \\ &-(\sin\phi_0\sin\phi_0)\bar{K}_{\phi\varepsilon} - (\sin\phi_0\cos\phi_0)\bar{K}_{\phi\phi} \end{aligned} \tag{118}$$

$$\begin{aligned}K_{xy} &= (\sin\phi_0\cos\phi_0)\bar{K}_{\varepsilon\varepsilon} - (\sin\phi_0\sin\phi_0)\bar{K}_{\varepsilon\phi} \\ &+(\cos\phi_0\cos\phi_0)\bar{K}_{\phi\varepsilon} - (\sin\phi_0\cos\phi_0)\bar{K}_{\phi\phi} \end{aligned} \tag{119}$$

$$\begin{aligned}K_{yy} &= (\cos\phi_0\cos\phi_0)\bar{K}_{\varepsilon\varepsilon} - (\sin\phi_0\cos\phi_0)\bar{K}_{\varepsilon\phi} \\ &-(\sin\phi_0\cos\phi_0)\bar{K}_{\phi\varepsilon} + (\sin\phi_0\sin\phi_0)\bar{K}_{\phi\phi} \end{aligned} \tag{120}$$

where

$$\bar{K}_{\varepsilon\varepsilon} = -Re\left(\frac{1}{2}\int_0^{2\pi}\int_0^1 \bar{P}_\varepsilon\cos\bar{\theta}\mathrm{d}\bar{\theta}\mathrm{d}\bar{z}\right), \tag{121}$$

$$\bar{K}_{\varepsilon\phi} = -Re\left(\frac{1}{2}\int_0^{2\pi}\int_0^1 \bar{P}_\varepsilon\sin\bar{\theta}\mathrm{d}\bar{\theta}\mathrm{d}\bar{z}\right), \tag{122}$$

$$\bar{K}_{\phi\epsilon} = -Re\left(\frac{1}{2}\int_0^{2\pi}\int_0^1 \bar{P}_\phi \cos\bar{\theta}\mathrm{d}\bar{\theta}\mathrm{d}\bar{z}\right) \tag{123}$$

$$\text{and } \bar{K}_{\phi\phi} = -Re\left(\frac{1}{2}\int_0^{2\pi}\int_0^1 \bar{P}_\phi \sin\bar{\theta}\mathrm{d}\bar{\theta}\mathrm{d}\bar{z}\right). \tag{124}$$

References

[1] Pecher O, Carretero-Gonzalez J, Griffith KJ, Grey CP. Materials' methods: NMR in battery research. Chem Mater 2017;29:213–42.
[2] Brunner E, Rauche M. Solid-state NMR spectroscopy: and advancing tool to analyse the structure and properties of metal-organic frameworks. Chem Sci 2020;11:4297–304.
[3] Lecoq L, Fogeron M-L, Meier BH, Nassal M, Böckmann A. Solid-state NMR for studying the structure and dynamics of viral assemblies. Viruses 2020;12:1069.
[4] Meier BH, Riek R, Böckmann A. Emerging structural understanding of amyloid fibrils by solid-state NMR. Trends Biochem Sci 2017;42(10).
[5] Andrew E, Bradbury A, Eades RG. Nuclear magnetic rotated spectra from a crystal rotated at high speed. Nature 1958;182:1659.
[6] Böckmann A, Ernst M, Meier BH. Spinning proteins, the faster, the better? J Magn Reson 2015;253:71–9.
[7] Andreas LB, Jaudzems K, Stanek J, Lalli D, Bertarello A, Marchand TL, Paepe DC, Kotelovica S, Akopjana I, Knott B, Wegner S, Engelke F, Lesage A, Emsley L, Tars K, Herrmann T, Pintacuda G. Structure of fully protonated proteins by proton-detected magic-angle spinning NMR. Proc Natl Acad Sci USA 2016;113(33):9187–92.
[8] Schledorn M, Malär A, Torosyan A, Penzel S, Klose D, Oss A, Org M-L, Wang S, Lecoq L, Cadalbert R, Samoson A, Böckmann A, Meier BH. Protein NMR spectroscopy at 150 kHz magic-angle spinning continues to improve resolution and mass sensitivity. Chembiochem 2020;21:2540–8.
[9] Herzog N, Wilhelm D, Koch S, Purea A, Osen D, Knott B, Engelke F. Aerodynamic optimization of a microturbine inserted in a magic-angle spinning system. J Fluids Eng 2016;138:1–16.
[10] Looser AE. Gas bearing with active magnetic damping for ultra-high-speed electrical drive systems (Ph.D. thesis), ETH Zurich; 2014.
[11] Rowe WB. Hydrostatic, aerostatic and hybrid bearing design. Elsevier; 2012.
[12] Lund JW. A theoretical analysis of whirl instability and pneumatic hammer for a rigid rotor in pressurized gas journal bearing. Trans ASME J Lubr Technol 1967;89(2):154–65.
[13] Wilhelm D, Purea A, Engelke F. Fluid flow dynamics in MAS systems. J Magn Reson 2015;257:51–63.
[14] Sesti EL, Alaniva N, Rand PW, Choi EJ, Albert BJ, Saliba EP, Scott FJ, Barnes AB. Magic angle spinning NMR below 6K with computational fluid dynamics analysis of fluid flow and temperature gradients. J Magn Reson 2018;286:1–9.
[15] Herzog N, Weber A, Purea A, Osen D, Knott B, Engelke F, Wilhelm D. Ultra low temperature microturbine for magic angle spinning system. J Fluids Eng 2022;144. 081205–1.
[16] Doty FD, Ellis PD. Design of high speed cylindrical NMR sample spinners. Rev Sci Instrum 1981;52:1868–75.
[17] Samoson A. H-MAS. J Magn Reson 2019;306:167–72.
[18] Szeri AZ. Fluid film lubrication. Cambridge University Press; 2010.
[19] Matsushita O, Tanaka M, Kanki H, Kobayashi M, Keogh P. Vibrations of rotating machinery. Springer; 2017.
[20] Vàsquez FGP. Model-based control design for flexible rotors supported by active gas bearings theory and experiment (Ph.D. thesis), Technical University of Denmark; 2016.
[21] San Andrés L. Gas film lubrication. Texas T & M Universities Digital Libraries; 2010.
[22] Wadhwa SS, Sinhasan R, Singh DV. Analysis of orifice compensated externally pressurized gas bearings. Tribol Int 1983;16(4):203–11.
[23] Lund JW. Review of the concept of dynamic coefficients for fluid film journal bearings. J Tribol 1987;109:37–41.
[24] Yang D, Chen C, Kang Y, Hwang R, Shyr S. Influence of orifices on stability of rotor-aerostatic bearing system. Tribol Int 2009;42:1206–19.
[25] Chen X-D, Zhu J-C, Chen H. Dynamic characteristics of ultra-precision aerostatic bearings. Adv Manuf 2013;1:82–6.
[26] Andrés LS. Hybrid flexure pivot-tilting pad gas bearings: Analysis and experimental validation. J Tribol 2006;128:551–8.
[27] Chen CH, Yang DW, Kang Y. Stability of rigid rotor-aerostatic bearings with double compensations caused by orifice and inherence in series. Tribol Int 2011;44:368–79.
[28] Mori A, Aoyama K, Mori H. Influence of the gas-film inertia forces on the dynamic characteristics of externally pressurized gas lubricated journal bearings. Bull JSME 1980;23:582–6.
[29] Mori A, Aoyama K, Mori H. Influence of the gas-film inertia forces on the dynamic characteristics of externally pressurized gas lubricated journal bearings. Bull JSME 1980;23:953–60.
[30] Hikichi K, Goto S, Togo S, Tanaka S, Isomura K. Hydroinertia gas bearings for micro spinners. J Micromech Microeng 2005;15:228–38.
[31] Isomura K, Tanaka S, Togo S, Esashi M. Development of high-speed micro-gas bearings for three-dimensional micro-turbo machines. J Micromech Microeng 2005;15:222–7.
[32] Otsu Y, Somaya K, Yoshimoto S. High-speed stability of a rigid rotor supported by aerostatic journal bearings with compound restrictors. Tribology International 2011;44:9–17.
[33] Ise T, Nakano S, Asami T, Endo Y, Honda I. Numerical analysis of hydroinertia gas bearings with inclined supply holes for high-speed rotary machines. Int J Mech Eng Appl 2014;2:52–7.
[34] Gross WA, Matsch LA, Castelli V, Eshel A, Vohr JH, Wildmann M. Fluid film lubrication. A Wiley-Interscience Publication; 1980.
[35] Chen CH, Yang DW, Kang Y, Hwang RM, Shyr SS. The influence of orifice restriction on the stability of rigid rotor-aerostatic bearing system. In: Proceedings of ASME turbo expo. Orlando, Florida, USA. 2009.